This is a preprint, the final version is subject to change, of the American Mineralogist (MSA)
Cite as Authors (Year) Title. American Mineralogist, in press.
DOI: https://doi.org/10.2138/am-2019-6661

Revision 2

Nature of hydrogen defects in clinopyroxenes from room temperature up to 1000 °C: Implication for the preservation of hydrogen in the upper mantle and impact on electrical conductivity

YAN YANG*[1], JANNICK INGRIN[2], QUNKE XIA[1], AND WENDI LIU[1]

[1]Institute of Geology and Geophysics, School of Earth Sciences, Zhejiang University, Hangzhou 310027, China

[2]Univ.Lille, CNRS, INRA, ENSCL, UMR 8207, UMET, Unité Matériaux et Transformations, F 59000 Lille, France

* Corresponding author
Institute of Geology and Geophysics
School of Earth Sciences
Zhejiang University
Hangzhou 310027, China

Email: yanyang2005@zju.edu.cn

ABSTRACT

Water incorporated as hydrogenated defects in mantle minerals can influence physical properties of the mantle. Knowledge of hydrogen defects at high temperatures (*T*) is fundamental to understand and quantify their influence on mantle physical properties. Clinopyroxene contributes significantly to the upper mantle water budget. Here, we investigate the behavior of hydrogen defects in ten natural clinopyroxene crystals at temperatures up to 1000 °C, using *in situ* and quenched experiments. The *in situ* high *T* Fourier transform infrared (FTIR) spectra indicate no proton transfer between point defects, but the local environments of hydrogen defects vary. Dehydration rates at 1000 °C of the six samples with different chemical compositions are calculated based on the quenched experiments. These rates are not only slightly site-specific, but also increase with Fe and tetrahedrally coordinated Al contents. Indeed, the Near-FTIR spectra suggest that the dehydration of the samples in this study involves oxidation of Fe^{2+}. For two diopsides with a mantle affinity, the diffusivity is about 10^{-12} m^2/s at 1000 °C. The results mainly have the following implications: (1) the different local environments of hydrogen defects between high *T* and low *T* may be responsible for the different mechanism of water impact on

electrical conductivity between high and low *T* experiments; (2) since the hydrogen diffusivities are positively related to Fe and ^{IV}Al contents, more care is required for interpretation of measured water concentrations for clinopyroxene samples with high Fe and ^{IV}Al contents. Compared between hydrogen diffusivities of olivine, orthopyroxene and clinopyroxene in mantle peridotite, clinopyroxene should be the most reliable recorder of water from depth.

Keywords: hydrogen defect, clinopyroxene, high temperature, diffusivity, *in situ* FTIR, electrical conductivity, effect mechanism

INTRODUCTION

The main minerals in the deep earth are nominally anhydrous minerals (NAMs), nevertheless, water can be incorporated as hydrogen defects which may strongly influence physical properties of NAMs, such as electrical conductivity, rheology and heat transferring (e.g., Mackwell et al. 1985; Karato 1990; Wang et al. 2006; Yoshino et al. 2008; Thomas et al. 2012; Faul et al. 2016; Chang et al. 2017), thereby affecting physical/chemical processes in the deep Earth (Peslier et al. 2010; Xia et al. 2013; Demouchy and Bolfan-Casanova 2016; Liu et al. 2017). However, the importance of water effect on several properties are still under current debates (e.g., Wang et al. 2006; Yoshino et al. 2006, 2008; Costa and Chakraborty 2008; Demouchy et al. 2012; Jones et al. 2012; Fei et al. 2013; Karato and Wang 2013; Yoshino and Katsura 2013; Dai and Karato 2015; Gardés et al. 2015). This is not only caused by differences in experimental methods, but also due to the complications in speciation of hydrogen defects (Karato 2015; Jones 2016). For instance, some recent experimental studies have reported that different hydrogen defects in NAMs have different effects on properties such as rheology and elasticity (e.g., Faul et al. 2016; Purevjav et al. 2016; Padrón-Navarta and Hermann 2017; Tielke et al. 2017). As a result, understanding speciation of hydrogen defects is fundamental to understand water effects on properties of NAMs. Theoretically, Karato (2006) speculated that speciation and sites of hydrogen defects in NAMs at high temperature may not be the same as those at room temperature. In fact, several studies have indicated that speciation of hydrogen

defects at room temperature may be misleading for discussing physical mechanism of water effects on properties of NAMs at high temperature. For example, Aines and Rossman (1985) reported that water speciation in feldspar at high temperature was different from that at room temperature. Yang and Keppler (2011) reported that hydrogen defects assigned to Si vacancies in olivine were unstable with increasing temperature. Yang et al. (2011) and Guo (2017) have reported that water speciation in rutile at room temperature is not representative of that at high temperatures relevant for subduction zones or upper mantle conditions. Yang et al. (2015) and Liu et al. (2018) found unquenchable transferring of hydrogen defects between sites in anorthoclase with increasing temperature. Very recently, Qin et al. (2018) has shown by numerical modeling that water speciation in olivine could be influenced by temperature and pressure. Consequently, knowledge of hydrogen defects in NAMs at high temperatures is essential to understand if water effects on mantle physical properties are significant at temperature and pressure conditions of Earth mantle.

In addition, different hydrogen defects have different diffusivities at high temperature. Recent experimental studies have reported site-specific hydrogen diffusivities for Ti-doped Fe-free olivine and clinopyroxene, respectively (Padrón-Navarta et al. 2014; Ferriss et al. 2016). Those works provide bases for distinguishing multiple processes in the history of an olivine grain (Tollan et al. 2015) and permit evaluating if water observed in upper mantle minerals is representative of the deep mantle (Denis et al. 2018). However, the recent study on naturally hydrated olivine did not report drastic difference in diffusivities for various hydrogen defects (Thoraval et al. 2018). Thus, the lack of consensus is a call for further study on site-specific hydrogen diffusion, especially in clinopyroxene.

Indeed, clinopyroxene is one of the main constituent minerals in the lower crust and upper mantle. Clinopyroxene is the pyroxene with large cations such as Ca^{2+}, Na^{+} and Li^{+} occupied in the M2 sites in the structure, thereby with space group C2/c at ambient conditions. For example, the diopside-hedenbergite solid solution, augite, jadeite, omphacite, spodumene and aegirine are clinopyroxene minerals. Among

them, the diopside and augite are calcic clinopyroxenes, jadeite, omphacite and aegirine are sodic clinopyroxenes, while spodumene is lithium aluminum silicate. Diopside is the main phase of the upper mantle peridotite. Hydrogen tends to partition into it rather than olivine and orthopyroxene (e.g., Aubaud et al. 2004; Grant et al. 2007; Demouchy et al. 2016). For diopside form mantle peridotite, water content ranges from 0 to 1000 wt. ppm (Demouchy et al. 2016). In addition, omphacite from mantle eclogite can contain water content up to 1800 ppm (Smyth et al. 1991). Yang et al. (2010, 2015) investigated the behavior of hydrogen defects in clinopyroxenes at temperatures between 20 and 500 °C. They found that the speciation and sites of hydrogen defects did not change over the temperature range, but the O-H bond stretching frequencies varied with different extent for different hydrogen defects. To date, defects in clinopyroxene under temperatures corresponding to the upper mantle remains unclear.

Consequently, in order to understand whether hydrogen defects observed at ambient conditions reflect their behavior at mantle temperatures, we investigated behavior of different hydrogen defects in clinopyroxenes at temperatures up to 1000 °C. Since nature of hydrogen defects is closely related to chemical environment, we chose ten clinopyroxene samples with different compositions (calcic and sodic clinopyroxenes, Fe-poor and Fe-rich clinopyroxenes) from various localities. We measured *in situ* Fourier transform infrared (FTIR) spectra of ten clinopyroxenes to monitor variations of hydrogen sites with increasing temperature. We also carried out quenched experiment at 1000 °C to determine hydrogen diffusivity of different OH groups. The Near-FTIR spectra of Fe^{2+} in the samples before and after dehydration were collected to qualify the dehydration mechanism. Those results provide information about what happens to hydrogen defects at atomic level during high temperature process, and contribute to further understanding preservation of hydrogen defects and their effect mechanisms on electrical conductivity at high temperatures.

MATERIALS AND METHODS

Sample description

Ten natural clinopyroxene single crystals from different localities were analyzed in this study: two gem-quality diopsides from Austria (diopside-Austria, with about 17 wt. ppm water) and Russia (diopside-Russia) which are previously described in Ingrin et al. (1989) and Andrut et al. (2007); a diopside in a marble xenolith from the Mount Marcy anorthosite massif at the Cascade Slide, New York, USA (diopside-marble), with 138 wt. ppm water reported in Johnson et al. (2002); two diopside crystals from Aksu, China (diopside-Aksu1, diopside-Aksu2), with 44 wt. ppm water reported in Shuai and Yang (2017); a diopside in peridotite xenolith hosted by Cenozoic basalt from Jiande, Zhejiang, China (diopside-JD), with 573 wt. ppm water reported in Hao et al. (2014); a diopside in peridotite xenolith (Mid-Atlantic Ridge) (diopside-deep sea, with 529 wt. ppm water, unpublished data); two augite megacrysts hosted by Cenozoic basalt from Yingfengling (augite-YFL) and Nushan (augite-NS), China, with less than 1 wt. ppm water reported by Yang and McCammon (2012); an omphacite from eclogites from the Roberts Victor kimberlite pipe, South Africa (omphacite), with 639 wt. ppm water reported by Huang et al. (2014). The samples are all C2/c clinopyroxenes (see the crystal structure data in the in the supplementary material). All samples were un-oriented and double polished single crystals. The samples with grain thickness ranging from 0.124 to 0.995 mm were used for the *in situ* high temperature FTIR spectra measurements. The samples with grain thickness ranging from 0.146 to 0.980 mm were used for the dehydration experiments.

Electron probe micro analyzer (EPMA)

The chemical compositions of the samples were determined using an EPMA 1600 (Shimadzu) electron microprobe at Zhejiang University (China). The analyses were performed with a 15 kV accelerating voltage, 10 nA beam current and a 5 μm beam diameter. Natural minerals were used as standards, and a program based on the ZAF procedure was applied for data correction. Multi-point measurements were conducted from core to rim of each mineral grain. The analyses demonstrate the chemical homogeneity of the samples. Reproducibility of multi-point analysis is <1% for elements with concentration >5% and <3% for elements with concentration >1%.

Based on the average chemical compositions, the calculated cations per 6 oxygen atoms are listed in Table 1.

In situ Mid-FTIR spectroscopy

Unpolarized and polarized FTIR spectra in the frequency range 4000-1000 cm^{-1} were collected using a Nicolet iS50 FTIR spectrometer coupled with a Continuμm microscope at Zhejiang University (China). A KBr beam-splitter and a liquid nitrogen-cooled MCT-A detector were used. A total of 128 scans were accumulated for each spectrum at a 4 cm^{-1} resolution. The squared aperture size was set to 50×50 μm. Background was collected at every temperature. Spectra were collected on the same selected area for each sample.

For the *in situ* high temperature measurements, the samples were placed on a Pt foil with a hole of 1.5 mm in diameter or on a sapphire plate in a heating stage with CaF_2 windows, equipped with a resistance heater and an S-type thermocouple. The sample was heated in N_2. The sample temperature was determined with an uncertainty of less than 1 °C. The temperature was increased from 20 to 1000 °C using a heating rate of 15 ˚C/min. For every temperature step, except otherwise indicated, the dwell time was 5 minutes.

Quenched dehydration experiments

We choose six clinopyroxene samples with different chemical composition for dehydration experiments. The experimental conditions and sample thickness are listed in Table 2. They were annealed in the heating stage at a desired temperature of 1000 ˚C for different hours, respectively. To avoid oxidation by the air, the heating stage was purged with N_2 of high purity during the annealing. Then FTIR measurements were carried out on the samples after quenching to room temperature.

Near-FTIR (NIR) spectroscopy

To investigate variations of Fe^{2+} in the samples before and after dehydration, NIR spectra in the frequency range 12000-4000 cm^{-1} were collected using a Bruker

Vertex70 FTIR spectrometer coupled with a hyperion1000 microscope at Zhejiang University (China). A CaF_2 beam-splitter and an InGaAs detector were used. A total of 64 scans were accumulated for each spectrum at a 4 cm^{-1} resolution. The squared aperture size was set to 50×50 μm. Spectra were collected on the same selected area for each sample.

Data analysis

For *in situ* experiment, to analyze site-specific temperature dependence of each OH band in the samples, spectra were decomposed using the Peakfit v4.12 software. Width, amplitude and frequency of every single band were adjustable to obtain the best peakfitting. For several samples with broad and significantly overlapped bands, we used OMNIC7.1 software to obtain the bulk integral absorbances, because peakfitting may not be the best way to extract absorbances (Zhang et al. 2007).

For the quenched experiment, we applied OMNIC7.1 software to obtain the bulk integral absorbance and calculate the bulk hydrogen diffusivity. Peakfit was used to obtain the integral absorbance of each OH band and calculate the site-specific hydrogen diffusivity. Based on dimensions of the samples, hydrogen diffusivities of the bulk hydrogen defects and site-specific hydrogen defect were obtained using the one-dimensional model of diffusion from Ingrin et al. (1995). In the calculation of OH concentration ratio of the final to initial concentration as a function of heating time, we used the ratio of the final to initial peak area, rather than the absolute water concentration. The resulting dehydration data were listed in Table 2.

RESULTS

Hydrogen defects at ambient conditions

As commonly observed in natural clinopyroxene (e.g., Skogby et al. 1990), four groups of OH absorption bands are found in the ten samples: 3620-3640 cm^{-1} (group 1), 3530-3540 cm^{-1} (group 2), 3460 cm^{-1} (group 3) and 3360 cm^{-1} cm^{-1} (group 4) as shown in Figure 1. Not every OH band is prominent in all samples because of the differences in thickness, chemical composition and crystallographic orientation of the

204 samples. Among the ten samples, the FTIR spectra of the diopside-Austria and
205 diopside-Russian, the diopside-marble, the diopside-Aksu have also been reported in
206 Ingrin et al. (1989), Johnson et al. (2002), Shuai and Yang (2017), respectively. It
207 should be noted that the band of group 1 at 3620-3640 cm^{-1} in omphacite may not be
208 intrinsic but related to nanometer-sized inclusions within the crystals (Koch-Müller et
209 al. 2004), thus we did not consider further this OH band of omphacite in the rest of the
210 study.

211 Cation substitutions usually cause shifts in band positions (Libowitzky and Beran
212 2006). Combined with the previously reported and some unpublished data of
213 clinopyroxene, positions of the OH bands of group 1 are plotted versus chemical
214 compositions in Figure 2. The band position correlates roughly with the amount of
215 tetrahedral coordinated Al^{3+} (^{IV}Al) (Fig. 2a, b). This supports the assignment of the
216 group 1 band to coupled substitution of Al^{3+} and H^{+} in Si vacancy (e.g., Skogby et al.
217 1990; Bromiley and Keppler 2004; Gavrilenko et al. 2010). To date, the band of group
218 2 lacks a clear compositional association. Some studies suggested that it was related
219 to substitution of H in M2 site or coupled substitution of H with some lower valence
220 cations in M1 site (Skogby et al. 1990; Bromiley and Keppler 2004), while
221 Koch-Müller et al. (2004) assigned it again to coupled substitution of Al^{3+} and H^{+} for
222 Si vacancy. Based on the relationship between OH frequencies and chemical
223 compositions, we further divide the group 2 OH band into the group 2a with OH
224 wavenumbers higher than 3535 cm^{-1} and the group 2b with OH wavenumbers lower
225 than 3535 cm^{-1} (Fig. 2b, c). The group 2a OH is related to tetrahedral coordinated Al^{3+},
226 which is consistent with the assignment in Koch-Müller et al. (2004). In agreement
227 with Skogby et al. (1990) and Bromiley and Keppler (2004), the group 2b OH could
228 be related to vacant M sites. Figure 2 also indicates that group 3 band may be related
229 to the vacant M site, consistent with the assignment of it to coupled substitution of H
230 and trivalent cation in M2 (Smyth et al. 1991; Koch-Müller et al. 2004; Stalder and
231 Ludwig 2007). The group 4 is rare in natural samples and only exists in the
232 diopside-Austria and diopside-Aksu2 in this study. These two diopsides have much

more M vacancies when compared to the others. It may be related to a higher M vacancy concentration than in other samples, thus supporting the assignment of H substitution in Mg vacancies (Stalder and Ludwig 2007). The negative vacancy may be due to the presence of ferric iron (Fe^{3+}) in these samples, which we neglected in the calculations. Indeed, the sample with the most negative vacancy is the Fe^{3+}-rich augite. Yang and McCammon (2012) reported that the augite-NS contains 34% of the total Fe as Fe^{3+}.

Behavior of hydrogen defects at high temperatures

OH bands at elevated temperatures

Figure 3 shows the unpolarized FTIR spectra of the clinopyroxenes at different temperatures (see the polarized FTIR spectra in the supplementary material). With increasing temperature, most bands gradually weaken, broaden and even diminish, especially for the bands at lower frequencies. A new OH band around 3443 cm^{-1} also appears in the spectra of the diopside-Austria and diopside-Aksu2 quenched from 1000 °C.

In Figure 4, site-specific band shifts with increasing temperature are reported. With increasing temperature, the band of group 1 linearly shifts to lower wavenumbers but to different extents for the studied samples, while the band of group 4 linearly shifts to higher wavenumbers. For most samples, the group 2 and group 3 bands significantly overlapped and disappeared at high temperatures, thus, we only display the data of samples with the prominent group 2 and group 3 bands. With increasing temperature, the group 2 and group 3 bands generally shift to lower wavenumbers, but not linearly or as drastically as the group 1 band does. The group 3 band of the diopside-Austria and diopside-Aksu2 shifts to higher wavenumbers with increasing temperature to 800 °C, then shift to lower wavenumbers.

Furthermore, there is a decrease in the absorption of the OH bands at elevated temperatures, especially for the augite-YFL and omphacite with almost no absorption at 1000 and 700 °C, respectively. Comparing between the FTIR spectra of the ten

261 samples before heated and after quenched from 1000 °C, it is clear that dehydration
262 has occurred during the heating process for most of the samples. In order to explore at
263 which temperature dehydration starts, we analyzed variations of the OH absorbances.
264 The evolution of the bulk integral absorbance of the OH bands with temperature is
265 shown in Figure 5. With increasing temperature, the bulk integral absorbance exhibits
266 little variation for the diopside-marble, while it displays a turning point with drastic
267 decrease at the temperature above 600 °C for the diopside-Austria, diopside-Aksu1,
268 diopside-JD, diopside-Russia, augite-YFL and augite-NS. In contrast, the turning
269 point appears earlier at 300 °C in the evolution of the bulk integral absorbance of OH
270 bands in the diopside-Aksu2 with temperature. Unfortunately, for most samples, the
271 OH bands significantly overlap at high temperatures. This impedes the accurate
272 analysis of absorbance of each OH band (Zhang et al. 2007). We choose the
273 diopside-Austria and diopside-Aksu2 with well separated OH bands and show their
274 site-specific evolution in Figure 5. The absorbances of the bands of group 1, group 3
275 and group 4 in the diopside-Austria keep steady, then drastically decrease at 700 ^{o}C.
276 For the diopsde-Aksu 2, the absorbances of the bands of group 3 and group 4 do not
277 change until increasing temperature to 500 and 700 ^{o}C, respectively, while the
278 absorbance of the group 2b band decrease first then increase with increasing
279 temperature to 700 ^{o}C.

280 **Hydrogen diffusivities at 1000^{o}C**

281 To investigate dehydration at high temperature, we conducted dehydration
282 experiments at 1000 ^{o}C on six samples with different chemical compositions. The
283 evolutions of the FTIR spectra with annealing time are shown in Figure 6. The bulk
284 and site-specific diffusion coefficients were obtained by fitting the data using a
285 one-dimensional model of diffusion as in Ingrin et al. (1995) and reported in Table 2.
286 The hydrogen diffusion coefficient is different not only between samples, but also
287 between hydrogen defects in the same sample. For example, the bulk hydrogen
288 diffusivities are the slowest in the diopside-marble and diopside-Russia ($6\text{-}7\times10^{-13}$
289 m^2/s), moderate in the diopsides from mantle peridotite (diopside-deep sea and

diopside-JD) (1×10^{-12} m^2/s), and the fastest in the diopside-Austria and augite-NS (6×10^{-12} m^2/s). Moreover, it seems that the site-specific hydrogen diffusivity is following different order between samples. For the diopside-marble, the diopside-Russia and the augite-NS, the diffusivity of hydrogen responsible for the OH band in group 1 is lower than that of the group 2. However, it is a little faster than that of the group 2 for the diopside-deep sea and diopside-JD. We have reported the bulk and site-specific diffusion coefficients as a function of chemical composition of the six samples in Figure 7. There are satisfying positive correlations between hydrogen diffusivities and chemical compositions except for the diopside-Austria. The presence of microscopic amphibole lamellae previously reported by Ingrin et al. (1989) in this sample could be a reason for its abnormal behavior. The lamellae provide possible shortcuts for diffusion. Excluding the diopside-Austria, the bulk and site-specific hydrogen diffusivities increase with the Fe and ^{IV}Al contents. The diffusivity of the group 1 OH is more correlated with ^{IV}Al content, while that of the group 2 OH is more correlated with Fe content. The bulk hydrogen diffusivity is more correlated with Fe than ^{IV}Al content. In contrast to the temperature dependence of O-H bond strength, we did not find any clear relationship between hydrogen diffusivity and its corresponding band frequency. Thus, the difference of chemical composition has much more effect on hydrogen diffusivity than the peak-specific difference does.

Variation of Fe^{2+} in the samples before and after dehydration

To explore the dehydration mechanism, Figure 8 compares the NIR spectra of the clinopyroxene samples before and after the dehydration experiments. The bands around 10,500 and 9500 cm^{-1} are assigned to crystal field bands (CFB) due to d-d transitions of Fe^{2+} at M1 and M2 sites, respectively (Rossi et al. 1987; Burns et al. 1993). After dehydration, the absorbances of Fe^{2+} at both M1 and M2 sites decrease for the diopside-Austria and diopside-Russia, while only the absorbances of Fe^{2+} at M2 sites decrease for the two diopsides from mantle peridotite and the augite-NS.

DISCUSSION

Variations of local environments of hydrogen defects with increasing temperature

The frequency of an OH band reflects the strength of O-H bond. The site-specific frequency shift of OH bands in clinopyroxene with increasing temperature indicates different local environments of the hydrogen defects within their structures. The negative frequency shifts of the group 1 OH bands indicate temperature-induced lengthening and weakening of O-H bonds. The positive frequency shifts of the group 4 OH bands suggest weakening of hydrogen bonds (H…O) with increasing temperature, because weakening of hydrogen bonds will induce a relative strengthening of the primary O-H bond (Nakamoto et al. 1955; Xu et al. 2013). The moderate negative frequency shifts of the groups 2 and 3 OH bands may indicate the simultaneous action of the lengthening of O-H and H…O bonds. One can speculate on a possible correlation between the initial frequency and its temperature dependence. We show the temperature dependence of OH frequency as a function of initial frequency for the clinopyroxene samples in this study and also for several minerals from previous studies for comparison in Figure 9a. A near linear relation exists between the temperature dependence of OH frequencies and their frequency at room temperature for silicate minerals. The room-temperature frequency corresponding to the cut-off between the positive and negative shift is around 3400 cm^{-1}. The low-temperature evolution of OH bands in forsterite also suggests this rough relationship (Ingrin et al. 2013). However, as shown in Figure 9a, the results for rutile do not lie along the trends probably due to the very different structures of silicate and oxide minerals.

In contrast to the resolved OH bands at room temperature, the IR spectra at 1000 ^{o}C display only one broad band. The one broad band at high temperature can arise from a statistical distribution across multiple sites or hydrogen disordering in the clinopyroxene structure. Based on the relationship between OH frequency and O-O distance (Libowitzky 1999), we can provide some constraints on the hydrogen bonding environments of hydrogen defects at room temperature and at 1000 ^{o}C

(Figure 9b). For the group 1 OH with frequencies around 3571-3553 cm^{-1} at 1000 ^{o}C, the predicted O-O distance is about 3.0 Å. For the group 2 OH with frequencies around 3510-3469 cm^{-1} at 1000 ^{o}C, respectively, the predicted O-O distance is about 2.9 Å. For the group 3 OH with frequencies around 3476-3417 cm^{-1} at 1000 ^{o}C, the predicted O-O distance is about 2.9-2.8 Å. For the group 4 OH with frequencies around 3398-3387 cm^{-1} at 700 ^{o}C, the predicted O-O distance is about 2.8 Å. Obviously, the O-O distances for the four groups OH at 1000 ^{o}C are more centralized than those observed at room temperature (Fig. 9c). Thus, the one broad band at high temperature such as 1000 ^{o}C is interpreted here as temperature-induced hydrogen disordering across multiple bonding sites with similar O-O distances. Temperature or pressure-induced hydrogen disordering was also expected in the structures of wadsleyite and ringwoodite (Kohn et al. 2002; Panero et al. 2013).

Site-specific thermal stability of the hydrogen defects

According to the Beer-Lambert relationship, $A = \varepsilon ct$, absorbance of O-H vibration relates to absorption coefficient of O-H, water concentration and sample thickness (ε is the absorption coefficient, A the measured integrated absorbance, t the sample thickness, and c the concentration of the molecule studied). Previous studies have shown that dehydration in diopside and augite could be neglected during the short heating process from room temperature to 500 °C (Yang et al. 2010, 2015). Additionally, contribution of the variation in sample thickness can be neglected below 500°C based on the thermal expansion of clinopyroxene (Pandolfo et al. 2015). Furthermore, *in situ* polarized FTIR spectra (see supplementary material) at elevated temperature indicate that O-H orientation does not significantly change with temperature. Thus, the slight variation before the turning point in the evolution of the integral absorbance with temperature indicates temperature dependence of OH absorption coefficient. According to Barron (1962), the absorption coefficient of a fundamental vibration transition is proportional to the square of the change of dipole moments. Extensive studies have suggested that absorbance coefficient of O-H in glasses and hydrous minerals is temperature dependent (e.g., Keppler and

Bagdassarov 1993; Withers et al. 1999; Zhang et al. 2007, 2016; Tokiwai and Nakashima 2010; Della Ventura et al. 2017). However, only few studies addressed temperature dependence of absorption coefficient of O-H vibration of hydrogen defects in NAMs (Yang et al. 2010, 2012, 2015).

In contrast to the slight variations at low temperatures, the dramatic decrease of the integral absorbance above the turning point at higher temperatures is due to dehydration. For most samples in this study, dehydration begins at temperatures above 600 °C. However, the diopside-Aksu2 starts dehydrating as early as 300 °C, while hydrogen defects in the diopside-marble are the most stable with negligible dehydration during the heating process. The dominant OH band belongs to the group 1 in the diopside-marble, while they belong to the groups 2, 3 and 4 in the diopside-Aksu2. It seems that the bands of group 1 are more stable than the ones of the other groups. Thus, it is expected that different hydrogen defects have distinct thermal stability. Indeed, in the diopside-Aksu2, dehydration of the group 3 starts at 500 °C, while the group 2b starts dehydrating at 200 °C and then re-hydrates at 700 °C. Dehydration of the group 4 starts at 700°C, which may account for the re-hydration of the group 2b. However, the group 1, group 3 and group 4 in the diopside-Austria start dehydrating at the same temperature. It is generally accepted that breaking of O-H bonds must occur during the dehydration. Therefore, we attempt to explain the different thermal stabilities of the hydrogen defects using the temperature dependence of O-H bond strength. Note that the O-H bond corresponding to the group 1 OH bands weakens, while that related to the group 4 OH bands strengthens with increasing temperature. Thus, it will be taken for granted that the hydrogen defects of the group 1 are most unstable defects, which was never demonstrated before. Consequently, the driving force for the dehydration remains complex.

Dehydration mechanism and origin of the band at 3443 cm^{-1}

Similar to Ferriss et al. (2016), we found that different hydrogen defects have different diffusivities. Ferriss et al. (2016) proposed that the hydrogen defects of the

group 2 OH band diffuse faster than those of the group 1 OH band based on their two diopside samples. Based on the data in this study, we do not find a uniform behavior of the diffusivities for different OH bands. In the diopside-marble, diopside-Russia and augite-NS, the hydrogen defects of the group 2 OH diffuse faster than those of the group 1, in agreement with Ferriss et al. (2016). However, in the two diopsides from mantle peridotite, the hydrogen defects of the group 2 OH band diffuse slightly slower than those of the group 1 OH band. But the difference between OH bands in clinopyroxene is not by more than one order of magnitude, far less than in Ti-doped Fe-free forsterite (Padrón-Navarta et al. 2014). In contrast, hydrogen diffusivities are mainly controlled by chemical compositions of the samples. Consistent with previous studies (Skogby and Rossman 1989; Ferriss et al. 2016), the bulk hydrogen diffusivities increase with Fe content (a.p.f.u.). For the two diopsides from mantle peridotites with Fe around 0.07-0.08 a.p.f.u., the bulk diffusivity is on the order of 10^{-12} at 1000 ^{o}C, one order of magnitude slower than the prediction of Ferriss et al. (2016). Contrary to Ferriss et al. (2016), we obtain a positive relationship between the bulk hydrogen diffusivities and ^{IV}Al content based on our data. We can further find relationships between site-specific hydrogen diffusivities and chemical compositions. For example, the diffusivity of hydrogen defects related to the group 1 OH band is more dependent on ^{IV}Al content, while that of the group 2 OH band is more dependent on Fe content. Thus, for the augite samples with high Fe and high ^{IV}Al, hydrogen defects diffuse very fast.

As for hydrogen diffusion mechanism, there are self-diffusion deduced from H-D exchange experiment, chemical diffusion controlled by the mobility of polarons and chemical diffusion controlled by the mobility of metal vacancies (Ingrin and Blanchard 2006). Among them, the mobility of polarons involves the oxidation-reduction of iron. In this study, the absorbances of Fe^{2+} decrease with dehydration. Thus, the dehydration mechanisms of the clinopyroxene samples involve oxidation of Fe^{2+}: $Fe^{2+} + OH^{-} = Fe^{3+} + O^{2-} + 1/2H_2$. That is just what we observed in relationship between hydrogen diffusivity and Fe content. Strictly speaking, the view

that extraction of H is a linear function of iron is an oversimplification. In fact, what is important is the number of Fe^{2+} available for the reaction. Based on the initial absorbances of Fe^{2+} in these samples, the content of Fe^{2+} is positively related to the bulk Fe content. Therefore, using bulk Fe content in this study does not significantly change the main results.

The band at 3443 cm^{-1} is not common in natural diopsides, but it has been previously observed in synthetic Fe- and Na-doped diopsides (Stalder and Ludwig 2007; Purwin et al. 2009). Based on the similar pleochroic behavior of the bands at 3360 and 3443 cm^{-1}, Purwin et al. (2009) assigned the band at 3443 cm^{-1} to a coupled substitution of a ferric iron and a proton to two neighboring Mg vacancies. Skogby and Rossman (1989) reported the new band around 3443 cm^{-1} appearing in the FTIR spectra of diopside from India after heating in H_2 or air and ascribed it to the lower frequency shift of the 3460 cm^{-1} band. Ferriss et al. (2016) also observed the increase of the band around 3443 cm^{-1} in the FTIR spectra of Kunlun diopside and Jaipur diopside after gently heating. They suggested that this additional hydrogen was taken up from the surroundings in the furnace, or was originally present in hydrous microinclusions, or initially distributed evenly among the various initial peaks. Thus, the origin of this new band has not been elucidated. In this study, the new band at 3443 cm^{-1} only occurs in the FTIR spectra of the diopside-Austria and Aksu2 quenched from high temperatures. Moreover, the 3443 cm^{-1} band seems to have an orientation similar to the band at 3460 cm^{-1} related to the group 3 (Figure 10b). Therefore, the band at 3443 cm^{-1} could be assigned to a new hydrogen defect in M site. To draw some relationships between this new hydrogen defect and hydrogen defects corresponding to other OH bands, variations of integral absorbances of the deconvoluted bands of the quenched sample with isothermal annealing time are plotted in Figure 10. With annealing time, the integral absorbance of the 3443 cm^{-1} band slightly increases, the integral absorbance of the 3467 cm^{-1} band shows little variation, while those of the 3645 and 3359 cm^{-1} bands decrease. As a result, it is unlikely that the hydrogen defect corresponding to the new band is related to

463 hydrogen defect corresponding to the 3467 cm^{-1} band. Since hydrogen defect
464 corresponding to the 3645 cm^{-1} band is located in Si site, it is most likely that the
465 3443 cm^{-1} band is related to hydrogen defect corresponding to 3359 cm^{-1} which is
466 located in M site. In contrast to other samples, only these two samples have the group
467 4 OH band at 3359 cm^{-1}, which also supports our conclusion. Since dehydration
468 mechanism of the diopside from Austria involved the oxidation of Fe^{2+} to Fe^{3+}, the
469 3443 cm^{-1} band could be a new hydrogen defect in M site, coupled with the ferric iron
470 formed during dehydration, in agreement with Purwin et al. (2009).

471 **IMPLICATIONS**

472 **Hydrogen speciation and sites in the clinopyroxene at high temperatures: effect**
473 **mechanism on electrical conductivity**

474 It is well established that hydrogen defects can influence electrical conductivity
475 of their host minerals. However, there are discrepancies among published
476 experimental results (e.g., Wang et al. 2006; Yoshino et al. 2006, 2008; Karato and
477 Wang 2013; Yoshino and Katsura 2013). In view of these long standing discrepancies,
478 Karato (2013, 2015) proposed a new theoretical model and suggested that the
479 rate-controlling diffusing species of hydrogen-assisted electrical conductivity are
480 different from those of H-D isotopic exchange. This model provides a good
481 explanation of some discrepancies among the different experimental observations at
482 different temperatures. Moreover, Dai and Karato (2014) showed by experiment that
483 the mechanism of electrical conductivity of olivine changed with temperature, which
484 is also observed for mantle clinopyroxene by Zhao and Yoshino (2016). Based on the
485 model of Karato (2013), they proposed that the diffusion of protons in M site is the
486 dominant contribution to electrical conductivity at high temperatures, while free
487 protons at low temperatures. Although these results are well explained by the model
488 (Karato 2013), there has been no direct observation of the changes of free protons at
489 low temperatures to two protons in M site at high temperatures.

490 FTIR spectra are good tracers for local environments of hydrogen defects. From

the *in situ* FTIR spectra at elevated temperatures in this study, we do not find a coupled growth and decline of OH bands as in rutile, anorthoclase or talc (Zhang et al. 2006; Yang et al. 2011, 2015; Guo 2017). This suggests that protons do not transfer easily between sites in the clinopyroxenes with increasing temperature up to 1000 ^{o}C. However, the local environments of hydrogen defects change with increasing temperature. At high temperatures, the four groups of hydrogen defects have similar O-O distances and display disordering in the structure. In contrast, the four groups of hydrogen defects have distinct O-O distances and show ordering in the structure at room *T*. Thus, it is unlikely that the water-effect on physical properties at high *T* is the same as that as low *T*. At high *T*, the strength of bonding between protons and the surrounding atoms are similar among the four groups of hydrogen defects. The protons belonging to the four groups of hydrogen defects likely have similar mobility at high *T*; this is likely not the case at low *T*. Therefore, the different local environments of hydrogen defects between high *T* and low *T* can be responsible for the different activation enthalpy of electrical conductivity between high and low *T* experiments observed by Dai and Karato (2014) and Zhao and Yoshino (2016). In addition, the pleochroism of hydrogen defects at high temperatures is not as prominent as at room temperature (see supplementary material). Thus, it can be inferred that anisotropy in electrical conductivity of clinopyroxene is also different between high and room temperature, which deserves to be tested in the future work.

This study extends the understanding of hydrogen speciation and sites in clinopyroxene at temperatures relevant to the lower crust and upper mantle. As conditions relevant of the deep Earth involve both high pressure and high *T*, the local environments of hydrogen defects in clinopyroxene at geologic conditions is simultaneously constrained by high pressure and high temperature. To date, no data have been reported for the high pressure behavior of hydrogen defects in clinopyroxene. Previous *in situ* high pressure spectroscopic investigations on olivine, wadsleyite and ringwoodite indicated that effect of pressure on variation in O-H bond strength is the contrary to the temperature effect (Cynn and Hofmeister 1994;

Jacobsen et al. 2005; Chamorro Pérez et al. 2006; Koch-Müller et al. 2011; Panero et al. 2013; Yang et al. 2014; Sakurai et al. 2015). Thus, it may be inferred the local environments of hydrogen defects in clinopyroxene at high temperature and high pressure is the same as ambient conditions. To fully address behavior of hydrogen defects in clinopyroxene under deep earth conditions, simultaneous *in situ* high temperature and high pressure FTIR spectroscopic investigations have to be carried out.

Preservation of hydrogen speciation and content in quenched clinopyroxene

Our *in situ* heating experiments indicate that hydrogen speciation in clinopyroxene does not change at least before dehydration. However, the dehydration experiments by quenching induced slight modifications of hydrogen speciation. In this case, a new band appears at 3443 cm^{-1}, which is linked to the dehydration process involving the oxidation of iron. Therefore, the occurrence of this band if observed in some natural clinopyroxenes could be used as a marker of a previous dehydration in oxidizing conditions.

The hydrogen diffusivities are positively related to Fe and ^{IV}Al contents in the clinopyroxene samples. Thus, for clinopyroxene samples with high Fe and ^{IV}Al contents, more care is required for interpretation of measured water concentrations. Based on the existing diffusivities of hydrogen in olivine and pyroxene, Denis et al. (2018) concluded that the remaining hydrogen concentrations observed in peridotites might only represent the “tip of the iceberg” of the water stored in the Earth's upper mantle. However, the hydrogen diffusivity in mantle-derived clinopyroxene was not available yet for referring in Denis et al. (2018). We provide here for the first time the hydrogen diffusivity at 1000 ^{o}C in the mantle-derived diopside, and we show that its diffusion coefficient may be one order of magnitude lower than that used in Denis et al. (2018). For the hydrogen diffusivity controlled by the proton-vacancy mechanism, it is similar and range between the diffusivities of olivine, enstatite and diopside, e.g., 6×10^{-12}, 1.3×10^{-11}, and 3.1×10^{-11} m^2/s at 1100^{o}C, respectively (Demouchy and Mackwell 2006; Carpenter Woods 2001; Ferriss et al. 2016). The similar diffusivities

cannot explain the mineral specific hydrogen concentrations in the mantle xenoliths. Therefore, the hydrogen diffusivity controlled by the proton-polaron mechanism may in fact contribute to a different preservation of hydrogen in the olivine, enstatite and diopside. In this study, the hydrogen diffusivity in the diopside samples is controlled by the proton-polaron mechanism. It ranges between 1×10^{-12} and 1.2×10^{-12} m^2/s at 1000 ^oC in the two diopsides from mantle peridotites, two orders of magnitude lower than 4×10^{-10} m^2/s in mantle olivine (Mackwell and Kohlstedt 1990), and slightly lower than 4×10^{-12} m^2/s in mantle enstatite (Carpenter Woods 2001) at the same temperature. It should be noted that the dehydration experiment in this study is carried out in open system and ambient pressure, thus, the hydrogen diffusivity may be lower than 10^{-12} m^2/s at 1000 ^oC in a closed system. As a result, clinopyroxene should be the most reliable recorder of water from depth compared with the mantle olivine and orthopyroxene, which was already inferred by Tian et al. (2016). Moreover, this study shows that the hydrogen diffusivity of the group 1 OH (3620-3640 cm^{-1}) increases with ^{IV}Al content, and that of the group 2 OH (3530-3540 cm^{-1}) increase with Fe content. For the two diopsides from mantle peridotites, the hydrogen diffusivity at 1000 ^oC of the group 1 OH (3640 cm^{-1}, with the hydrogen diffusivity of 1.6×10^{-12}) is slightly higher than that of the group 2 OH (3540 cm^{-1}, with the hydrogen diffusivity of 1.2×10^{-12}). This site-specific difference is quite low and much less than the difference caused by chemical composition. Therefore, preservation of water in mantle clinopyroxene mainly depends on chemical composition.

ACKNOWLEDGMENTS

This work was supported by the Fundamental Research Funds for the Central Universities (2016QNA3014, 2017QNA3015) and Zhejiang Province Natural Science Foundation of China (LY18D020001). Shun-ichiro Karato is thanked for discussion. Xiaozhi Yang is thanked for providing the diopside samples from Aksu. Pei Li is thanked for providing the omphacite sample and the diopside sample from Mid-Atlantic ridge.

REFERENCES

578 Aines, R.D., and Rossman, G.R. (1985) The high temperature behavior of trace
579 hydrous components in silicate minerals. American Mineralogist, 70, 1169-1179.

580 Andrut, M., Wildner, M., Ingrin, J., and Beran, A. (2007) Mechanisms of OH defect
581 incorporation in naturally occurring, hydrothermally formed diopside and jadeite.
582 Physics and Chemistry of Minerals, 34, 543-549.

583 Aubaud, C., Hauri, E.H., and Hirschmann, M.M. (2004) Hydrogen partition
584 coefficients between nominally anhydrous minerals and basaltic melts.
585 Geophysical Research Letters, 31 (20).

586 Barrow, G.M. (1962) Introduction to molecular spectroscopy. Mc-Graw-Hill, New
587 York, 76-80.

588 Bromiley, G.D., and Keppler, H. (2004) An experimental investigation of hydroxyl
589 solubility in jadeite and Na-rich clinopyroxenes. Contributions to Mineralogy
590 and Petrology, 147, 189-200.

591 Burns, R.G. (1993) Mineralogical applications of crystal field theory, 2nd edn.
592 Cambridge University Press, Cambridge.

593 Carpenter Woods, S. (2001) The Kinetics of Hydrogen Diffusion in Single Crystal
594 Orthopyroxene. (PhD thesis). Dept. Geosciences. Pennsylvania State University.

595 Chamorro Pérez, E.M., Daniel, I., Chervin, J.C., Dumas, P., Bass, J.D., and Inoue, T.
596 (2006) Synchrotron IR study of hydrous ringwoodite (γ-Mg_2SiO_4) up to 30 GPa.
597 Physics and Chemistry of Minerals, 33, 502-510.

598 Chang, Y.Y., Hsieh, W.P., Tan, E., and Chen, J.H. (2017) Hydration-reduced lattice
599 thermal conductivity of olivine in Earth's upper mantle. Proceedings of the
600 National Academy of Sciences of the United States of America, 114, 4078.

601 Costa, F., and Chakraborty, S. (2008) The effect of water in Si and O diffusion rates in
602 olivine and implications for the transport properties and processes in the upper
603 mantle. Physics of the Earth and Planetary Interiors, 166, 11-29.

604 Cynn, H., and Hofmeister, A.M. (1994) High-pressure IR spectra of lattice modes and

605 OH vibrations in Fe-bearing wadsleyite. Journal of Geophysical Research, 99,
606 17717-17727.

607 Dai, L., and Karato, S. (2014) High and highly anisotropic electrical conductivity of
608 the asthenosphere due to hydrogen diffusion in olivine. Earth and Planetary
609 Science Letters, 408, 79-86.

610 Dai, L., and Karato, S. (2015) Reply to comment on "High and highly anisotropic
611 electrical conductivity of the asthenosphere due to hydrogen diffusion in olivine"
612 by Dai and Karato [Earth Planet. Sci. Lett. 408 (2014) 79-86]. Earth and
613 Planetary Science Letters, 427, 300-302.

614 Della Ventura, G., Susta, U., Bellatreccia, F., Marcelli, A., Redhammer, G.J., and
615 Oberti, R. (2017) Deprotonation of Fe-dominant amphiboles: Single-crystal
616 HT-FTIR spectroscopic studies of synthetic potassic-ferro-richterite. American
617 Mineralogist, 102, 117-125.

618 Demouchy, S., and Mackwell, S. (2006) Mechanisms of hydrogen incorporation and
619 diffusion in iron-bearing olivine. Physics and Chemistry of Minerals, 33,
620 347-355.

621 Demouchy, S., Tommasi, A., Barou, F., Mainprice, D., and Cordier, P. (2012)
622 Deformation of olivine in torsion under hydrous conditions. Physics of the Earth
623 and Planetary Interiors, 202-203, 75-70.

624 Demouchy, S., and Bolfan-Casanova, N. (2016) Distribution and transport of
625 hydrogen in the lithospheric mantle: A review. Lithos, 240-243, 402-425.

626 Demouchy, S., Thoraval, C., Bolfan-Casanova, N., and Manthilake, G. (2016)
627 Diffusivity of hydrogen in iron-bearing olivine at 3 GPa. Physics of the Earth
628 and Planetary Interiors, 260, 1-13.

629 Denis, C.M.M., Demouchy, S., and Alard, O., (2018) Heterogeneous hydrogen
630 distribution in orthopyroxene from veined mantle peridotite (San Carlos,
631 Arizona): Impact of melt-rock interactions. Lithos, 302-303, 298-311.

632 Faul, U., Cline, C.J., David, E.C., Berry, A.J., and Jackson, I. (2016)
633 Titanium-hydroxyl defect-controlled rheology of the Earth's upper mantle. Earth

634 and Planetary Science Letters, 452, 227-237.

635 Fei, H., Wiedenbeck, M., Yamazaki, D., and Katsura, T. (2013) Small effect of water
636 on uppermantle rheology based on silicon self-diffusion coefficients. Nature,
637 213-215.

638 Ferriss, E., Plank, T., and Walker, D. (2016) Site-specific hydrogen diffusion rates
639 during clinopyroxene dehydration. Contributions to Mineralogy and Petrology,
640 171, 1-24.

641 Gardés, E., Gaillard, F., and Tarits, P. (2015) Comment to "High and highly
642 anisotropic electrical conductivity of the asthenosphere due to hydrogen
643 diffusion in olivine" by Dai and Karato [Earth Planet. Sci. Lett. 408 (2014)
644 79-86]. Earth and Planetary Science Letters, 427, 296-299.

645 Gavrilenko, P., Ballaran, T.B., and Keppler, H. (2010) The effect of Al and water on
646 the compressibility of diopside. American Mineralogist, 95, 608-616.

647 Grant, K., Ingrin, J., Lorand, J.P., and Dumas, P. (2007) Water partitioning between
648 mantle minerals from peridotite xenoliths. Contributions to Mineralogy and
649 Petrology, 154 (1), 15-34.

650 Guo, H. (2017) In-situ infrared spectra of OH in rutile up to 1000°C. Physics and
651 Chemistry of Minerals, DOI 10.1007/s00269-017-0881-6.

652 Hao, Y.T., Xia, Q.K., Li, Q.W., Chen, H., and Feng, M. (2014) Partial melting control
653 of water contents in the Cenozoic lithospheric mantle of the Cathaysia block of
654 South China. Chemical Geology, 380, 7-19.

655 Hao, Y.T., Xia, Q.K., Jia, Z.B., Zhao, Q.C., Li, P., Feng, M., and Liu, S.C. (2016)
656 Regional heterogeneity in the water content of the Cenozoic lithospheric mantle
657 of Eastern China. Journal of Geophysical Research-solid Earth, 121, 517-537.

658 Huang, J.X., Li, P., Griffin, W.L., Xia, Q.K., Greau, Y., Pearson, N.J., and O'Reilly,
659 S.Y. (2014) Water contents of Roberts Victor xenolithic eclogites: primary and
660 metasomatic controls. Contributions to Mineralogy and Petrology, 168, 1092.

661 Ingrin, J., Latrous, K., Doukhan, J.C., and Doukhan, N. (1989) Water in diopside: An
662 electron microscopy and infrared spectroscopy study. European Journal of
663 Mineralogy, 1, 327-341.

664 Ingrin, J., Hercule, S., and Charton, T. (1995) Diffusion of hydrogen in diopside:
665 Results of dehydration experiments. Journal of Geophysical Research, 100,
666 15489-15499.

667 Ingrin, J., and Blanchard, M. (2006) Diffusion of Hydrogen on Minerals. Review of
668 Mineralogy & Geochemistry, 62, 291-320.

669 Ingrin, J., Liu, J., Depecker, C., Kohn, S.C., Balan, E., and Grant, K.J. (2013)
670 Low-temperature evolution of OH bands in synthetic forsterite, implication for
671 the nature of H-defects at high pressure. Physics and Chemistry of Minerals, 40,
672 499-510.

673 Jacobsen, S.D., Demouchy, S., Frost, D.J., Ballaran, T.B., and Kung, J. (2005) A
674 systematic study of OH in hydrous wadsleyite from polarized FTIR spectroscopy
675 and single-crystal X-ray diffraction: Oxygen sites for hydrogen storage in Earth's
676 interior. American Mineralogist, 90, 61-70.

677 Johnson, E.J., Rossman, G.R., Dyar, M.D., and Valley, J.W. (2002) Correlation
678 between OH concentration and oxygen isotope diffusion rate in diopsides from
679 the Adirondack mountains New York. American Mineralogist, 87, 899-908.

680 Jones, A.G., Fullea, J., Evans, R.L., and Muller, M.R. (2012) Water in cratonic
681 lithosphere: calibrating laboratory-determined models of electrical conductivity
682 of mantle minerals using geophysical and petrological observations.
683 Geochemistry Geophysics Geosystems, 13, 360-366.

684 Jones, A. (2016) Proton conduction and hydrogen diffusion in olivine: an attempt to
685 reconcile laboratory and field observations and implications for the role of grain
686 boundary diffusion in enhancing conductivity. Physics and Chemistry of
687 Minerals, 43, 237-265.

688 Karato, S. (1990) The role of hydrogen diffusivity in the electrical conductivity of the
689 upper mantle. Nature, 347, 272 – 273.

690 Karato, S. (2006) Influence of hydrogen-related defects on the electrical conductivity
691 and plastic deformation of mantle minerals: a critical review. In Earth's Deep
692 Water Cycle vol. 168, American Geophysical Union, Washington D.C.

693 Karato, S. (2013) Theory of isotope diffusion in a material with multiple species and
694 its implications for hydrogen-enhanced electrical conductivity in olivine. Physics
695 of Earth Planetary Interiors, 219, 49-54.

696 Karato, S., and Wang, D. (2013) Electrical conductivity of minerals and rocks. In:
697 Karato, S. (Ed.), Physics and Chemistry of the Deep Earth. Wiley-Blackwell,
698 New York, pp. 145-182.

699 Karato, S. (2015) Some notes on hydrogen-related point defects and their role in the
700 isotope exchange and electrical conductivity in olivine. Physics of the Earth and
701 Planetary Interiors, 248, 94-98.

702 Keppler, H., and Bagdassarov, N.S. (1993) High-temperature FTIR spectra of H_2O in
703 rhyolite melt to 1300 °C. American Mineralogist, 78, 1324-1327.

704 Koch-Müller, M., Matsyuk, S., and Wirth, B. (2004) Hydroxyl in omphacites and
705 omphacitic clinopyroxenes of upper mantle to lower crystal origin beneath the
706 Siberian platform. American Mineralogist, 89, 921-931.

707 Koch-Müller, M., Speziale, S., Deon, F., Mrosko, M., and Schade, U. (2011) Stress
708 induced proton disorder in hydrous ringwoodite. Physics and Chemistry of
709 Minerals, 38, 65-73.

710 Kohn, S.C., Brooker, R.V., Frost, D.J., Slesinger, A.E., and Wood, B.G. (2002)
711 Ordering of hydroxyl defects in hydrous wadsleyite (β-Mg_2SiO_4). American
712 Mineralogist, 87, 293-301.

713 Libowitzky, E. (1999) Correlation of O-H stretching frequencies and O-H…O
714 hydrogen bond lengths in minerals. Monatsh Chem, 130, 1047-1059.

715 Libowitzky, E., and Beran, A. (2006) The structure of hydrous species in nominally
716 anhydrous minerals: information from polarized IR spectroscopy. Review of

717 Mineralogy & Geochemistry, 62, 29-52.

718 Liu, J., Xia, Q.K., Kuritani, T., Hanski, E., and Yu, H.R. (2017) Mantle hydration and
719 the role of water in the generation of large igneous provinces. Nature
720 Communications, 8, 1824.

721 Liu, W.D., Yang, Y., Zhu, K., and Xia, Q.K. (2018) Temperatue dependecnes of
722 hydrous species in feldspars. Physics and Chemistry of Minerals,
723 https://doi.org/10.1007/s00269-018-0946-1.

724 Mackwell, S.J., Kohlstedt, D.L., and Paterson, M.S. (1985) The role of water in the
725 deformation of olivine single crystals. Journal of Geophysical Research, 90,
726 11319 – 11333.

727 Mackwell, S.J., and Kohlstedt, D.L. (1990) Diffusion of hydrogen in olivine:
728 implications for water in the mantle. Journal of Geophysical Research, 95,
729 5079-5088.

730 Nakamoto, K., Margosches, M., and Rundle, R.E. (1955): Stretching frequencies as a
731 function of distances in hydrogen bonds. Journal of the American Chemical
732 Society, 77, 6480-6486.

733 Padrón-Navarta, J.A., Hermann, J., and O'Neill, H.S.C. (2014) Site-specific hydrogen
734 diffusion rates in forsterite. Earth and Planetary Science Letters, 392, 100-112.

735 Pandolfo, F., Cámara, F., Domeneghetti, M.C., Alvaro, M., Nestola, F., Karato, S.,
736 and Amulele, G. (2015) Volume thermal expansion along the jadeite-diopside
737 join. Physics and Chemistry of Minerals, 42, 1-14.

738 Panero, W.R., Smyth, J.R., Pigott, J.S., Liu, Z., and Frost, D.J. (2013). Hydrous
739 ringwoodite to 5 K and 35 GPa: Multiple hydrogen bonding sites resolved with
740 FTIR spectroscopy. American Mineralogist, 98, 637-642.

741 Peslier, A.H., Woodland, A.B., Bell, D.R., and Lazarov, M. (2010) Olivine water
742 contents in the continental lithosphere and the longevity of cratons. Nature, 467,
743 78-U108.

744 Purevjav, N., Okuchi, T., Tomioka, T., Wang, X., and Hoffmann, C. (2016)
745 Quantitative analysis of hydrogen sites and occupancy in deep mantle hydrous
746 wadsleyite using single crystal neutron diffraction. Scientific Report, DOI:
747 10.1038/srep34988.

748 Purwin, H., Stalder, R., and Skogby, H. (2009) Hydrogen incorporation in Fe- and
749 Na-doped diopsides. European Journal of Mineralogy, 21(4), 691-704.

750 Padrón, J.A., and Hermann, J. (2017) A Subsolidus Olivine Water Solubility Equation
751 for the Earth's Upper Mantle. Journal of Geophysical Research: Solid Earth, DOI:
752 10.1002/2017JB014510.

753 Qin, T., Wentzcovitch R.M., Umemoto, K., Hirschmann, M.M., and Kohlstedt, D.L.
754 (2018) Ab initio study of water speciation in forsterite: Importance of the
755 entropic effect. American Mineralogist, 103, 692-699.

756 Rossi, G., Oberti, R., Dal, N.A., Molin, G.M., and Mellini, M. (1987) Residual
757 electron density at the M2 site in C2/c clinopyroxenes; relationships with bulk
758 chemistry and sub-solidus evolution. Physics and Chemistry of Minerals, 14,
759 514-520.

760 Sakurai, M., Tsujino, N., Tateno, S., Suzuki, T., Yoshino, T., Kawamura, K., and
761 Takahashi, E. (2015) In situ high pressure IR spectroscopic observations on the
762 upper mantle anhydrous minerals using diamond anvil cell. Japan Geoscience
763 Union Meeting.

764 Shuai, K., and Yang, X.Z. (2017) Quantitative analysis of H-species in anisotropic
765 minerals by polarized infrared spectroscopy along three orthogonal directions.
766 Contributions to Mineralogy and Petrology, 172, 14.

767 Skogby, H., and Rossman, G.R. (1989) OH^- in pyroxene: An experimental study of
768 incorporation mechanisms and stability. American Mineralogist, 74, 1059-1069.

769 Skogby, H., Bell, D.R., and Rossman, G.R. (1990) Hydroxide in pyroxene: variations
770 in the natural environment. American Mineralogist, 75, 767-774.

771 Smyth, J.R., Bell, D.R., and Rossman, G.R. (1991) Incorporation of hydroxyl in
772 upper-mantle clinopyroxenes. Nature, 351, 732-735.

773 Stalder, R., and Ludwig, T. (2007) OH incorporation in synthetic diopside. European
774 Journal of Mineralogy, 19(3), 373-380.

775 Thomas, S.M., Bina, C.R., Jacobsen, S.D., and Goncharov, A.F. (2012) Radiative heat
776 transfer in a hydrous mantle transition zone. Earth and Planteary Science Letters,
777 357, 130-136.

778 Thoraval, C., Demouchy, S., and Padrón, J.A. (2018) Relative diffusivities of hydrous
779 defects from partially dehydrated natural olivine. Physics and Chemistry of
780 Minerals. DOI: https://doi.org/10.1007/s00269-018-0982-x.

781 Tian, Z.Z., Liu, J., Xia, Q.K., Ingrin, J., Hao, Y.T., and Christophe, D. (2016) Water
782 concentration profiles in natural mantle orthopyroxenes: A geochronometer for
783 long annealing of xenoliths within magma. Geology, G38620.1

784 Tielke, J.A., Zimmerman, M.E., and Kohlstedt, D.L. (2017). Hydrolytic weakening in
785 olivine single crystals. Journal of Geophysical Research, 122, 3465-3479.

786 Tokawai, K., and Nakashima, S. (2010) Dehydration kinetics of muscovite by in situ
787 infrared microspectroscopy. Physics and Chemistry of Minerals, 37, 91-101.

788 Tollan PME, O'Neill HSC, Hermann J, Benedictus A, and Arculus RJ (2015) Frozen
789 melt-rock reaction in a peridotite xenolith from sub-arc mantle recorded by
790 diffusion of trace elements and water in olivine. Earth and Planetary Science
791 Letters, 422, 169-181.

792 Wang, D.J., Mookherjee, M., and Xu, Y.S. (2006) The effect of water on the electrical
793 conductivity of olivine. Nature, 443, 977-980.

794 Withers, A.C., and Behrens, H. (1999) Temperature-induced changes in the NIR
795 spectra of hydrous albitic and rhyolitic glasses between 300 and 100K. Physics
796 and Chemistry of Minerals, 27, 119-132.

797 Xia, Q.K., Liu, J., Liu, S.C., Kovács, I., Feng, M., and Dang, L. (2013) High water
798 content in Mesozoic primitive basalts of the North China Craton and implications
799 on the destruction of cratonic mantle lithosphere. Earth and Planetary Science
800 Letters, 361, 85-97.

801 Xu, H., Zhao, Y., Hickmott, D.D., Lane, N.J., Vogel, S.C., Zhang, J., and Daemen, L.L.
802 (2013) High-temperature neutron diffraction study of deuterated brucite. Physics
803 and Chemistry of Minerals, 40, 799-810.

804 Yang, X.Z., Xia, Q.K., Deloule, E., Dallai, L., Fan, Q.C., and Feng, M. (2008) Water
805 in minerals of the continental lithospheric mantle and overlying lower crust: A
806 comparative study of peridotite and granulite xenoliths from the North China
807 Craton. Chemical Geology, 256, 33-45.

808 Yang, X.Z., and Keppler, H. (2011) In-situ infrared spectra of OH in olivine to 1100℃.
809 American Mineralogist, 96, 451-454.

810 Yang, X.Z., and McCammon, C. (2012) Fe^{3+}-rich augite and high electrical
811 conductivity in the deep lithosphere. Geology, 2, 131-134.

812 Yang, X.Z., Keppler, H., Dubrovinsky, L, and Kurnosov, A. (2014) In-situ infrared
813 spectra of hydroxyl in wadsleyite and ringwoodite at high pressure and high
814 temperature. American Mineralogist, 99, 724-729.

815 Yang, Y., Xia, Q., Feng, M., and Zhang, P. (2010) Temperature dependence of IR
816 absorption of OH species in clinopyroxene. American Mineralogist, 95,
817 1439-1443.

818 Yang, Y., Xia, Q., Feng, M., and Gu, X.Y. (2011) In situ varying temperature FTIR
819 experiment study of rutile. American Mineralogist, 96, 1851-1855.

820 Yang, Y., Xia, Q., Feng, M., and Liu, S. (2012) OH in nature orthopyroxene: an in situ
821 FTIR investigation at varying temperatures. Physics and Chemistry of Minerals,
822 39, 413-418.

823 Yang, Y., Xia, Q., and Zhang, P. (2015) Evolutions of OH groups in diopside and

feldspars with temperature. European Journal of Mineralogy, 27, 185-192.

Yoshino, T., Matsuzaki, T., Yamashita, S., and Katsura, T. (2006) Hydrous olivine unable to account for conductivity anomaly at the top of the asthenosphere. Nature, 443, 973-976.

Yoshino, T., Manthilake, G., Matsuzaki, T., and Katsura, T. (2008) Dry mantle transition zone inferred from the conductivity of wadsleyite and ringwoodite. Nature, 451, 326-329.

Yoshino, T., and Katsura, T. (2013) Electrical conductivity of mantle minerals: role of water in conductivity anomalies. Annual Review of Earth and Planetary Sciences, 41, 605-628.

Zhao, C.C., and Yoshino, T. (2016) Electrical conductivity of mantle clinopyroxene as a function of water content and its implication on electrical structure of uppermost mantle. Earth and Planetary Science Letters, 447, 1-9.

Zhang, M., Hui, Q., Lou, X.J., Redrern, S.A.T., Salje, E.K.H., and Tarantino, S.C. (2006) Dehydroxylation, proton migration, and structural changes in heated talc: An infrared spectroscopic study. American Mineralogist, 91, 816-825.

Zhang, M., Salje, E. K. H., Carpenter, M. A., Wang, J.Y., Groat, L. A., Lager, G. A., Wang, L., Beran, A., and Bismayer, U. (2007) Temperature dependence of IR absorption of hydrous/hydroxyl species in minerals and synthetic materials. American Mineralogist, 92, 1502-1517.

Zhang, M., Tarantino, S.C., Su, W., Lou, X., and Ren, X. (2016) Phonons, OH vibrations ans structural modifications of phlogopite at high temperatures: an in-situ infrared spectroscopic study. American Mineralogist, 101, 1873-1883.

Figure captions

FIGURE 1.Unpolarized FTIR spectra of OH in the ten clinopyroxenes at room temperature. The spectra are shifted for clarity. The positions of the four groups OH bands are indicated by dotted lines: red lines indicate the group 1 OH; blue lines indicate the group 2 OH; green lines indicate the group 2 OH; black lines indicate the

852 group 4 OH.

853 FIGURE 2. Relationship between OH frequencies and chemical compositions in
854 the clinopyroxenes: (a) Wavenumbers of the group 1 OH band as a function of
855 tetrahedral coordinated Al^{3+} content in atoms per formula unit (a.p.f.u.). The data of
856 diopside (YT-25, peridotite) is from Hao et al. (2016), the data of diopside (NS-16,
857 peridotite) and diopside (NS-29, peridotite) are from Yang et al. (2008). The data of
858 augite and diopside (GRR04, granulite) are unpublished data; (b) Wavenumbers of the
859 group 2a OH band as a function of tetrahedral coordinated Al^{3+} content in atoms per
860 formula unit (a.p.f.u.); (c) Wavenumbers of the group 2b OH band as a function of M
861 vacancies; (d) Wavenumbers of the group 3 OH band as a function of M vacancies.
862 The M vacancy is a first approximation since the calculation is very simple neglecting
863 Fe^{3+}.

864 FIGURE 3. In situ unpolarized FTIR spectra of OH in the ten clinopyroxenes at
865 high temperatures. The room-temperature positions of the OH bands are indicated by
866 dotted lines. The arrow indicates the appearance of the new band at 3443 cm^{-1} in the
867 diopside-Austria and diopside-Aksu2. The spectra are shifted for clarity.

868 FIGURE 4. Plots of frequency of the OH bands of clinopyroxenes against
869 temperature: (a) group 1; (b) group 2a; (c) group 2b; (d) group 3; (e) group 4

870 FIGURE 5. Variation of the integral absorbances of the OH bands with
871 temperature: (a) The bulk integral absorbances; (b) The individual integral absorbance
872 of each OH band. The dotted lines indicate the turning points at which dehydration
873 starts.

874 FIGURE 6. Room-temperature unpolarized FTIR spectra of the samples
875 annealed in N_2 at 1000^{o}C.

876 FIGURE 7. Hydrogen diffusivities during dehydration as a function of Fe and
877 ^{IV}Al content in atoms per formula unit (a.p.f.u.): (a) Bulk and site-specific hydrogen
878 diffusivities vs. Fe content; (b) Bulk and site-specific hydrogen diffusivities vs. ^{IV}Al
879 content; (c) Bulk hydrogen diffusivities vs. Fe content excluding the diopside-Austria;
880 (d) Bulk hydrogen diffusivities vs. ^{IV}Al content excluding the diopside-Austria.

881 FIGURE 8. Unpolarized NIR spectra of the samples normalized to 1 cm of
882 thickness before and after dehydration. The arrows indicate the absorptions of Fe^{2+}.

883 FIGURE 9. (a) Relationship between temperature dependence of OH frequency
884 shift and room-temperature frequency. The blue symbols are the data from this study
885 and the black symbols are the data from the literature. (b) Correlation between O-H
886 stretching frequency and O-H…O distance of the four groups of OH. The black
887 symbols indicate the data at room temperature, and the blue symbols indicate the data
888 at 1000 ^{o}C. For each group of OH in the ten samples, the highest and lowest
889 frequencies were chosen. (c) The comparison of ranges of O-H…O distance of the
890 four groups of OH between room temperature and 1000 ^{o}C.

891 FIGURE 10. (a) Unpolarized FTIR spectra of OH in the diopside from Austria
892 recorded at room temperature before heating and after annealing at 800 and 900 ^{o}C for
893 different time. The dotted lines indicate the new band at 3443 cm^{-1}. The spectra are
894 shifted for clarity. (b) Room-temperature polarized FTIR spectra of OH in diopside
895 from Austria after annealing at 900 ^{o}C for 30 min with polarizer rotating 0^{o} and 90^{o}. (c)
896 Plots of integral absorbance of the deconvoluted OH bands of the diopside from
897 Austria against annealing time at 800 ^{o}C (integral absorbance of the FTIR spectrum
898 before heating was used as the initial value). (d) Integral absorbance of the
899 deconvoluted OH bands of the diopside from Austria against annealing time at 900
900 ^{o}C.

901

902

903

904

905

906

This is a preprint, the final version is subject to change, of the American Mineralogist (MSA)
Cite as Authors (Year) Title. American Mineralogist, in press.
DOI: https://doi.org/10.2138/am-2019-6661

907 **Table 1** Cation proportions as calculated from electron microprobe analyses of
908 clinopyroxenes.

	Diopside-Austria	Diopside-marble	Diopside-JD	Augite-YFL	Omphacite	Diopside-Aksu	Diopside-Russia	Diopside-deep sea	Augite-NS
K	0.000	0.000	0.000	0.000	0.000	0.000	0.000	0.000	0.000
Na	0.003	0.001	0.135	0.119	0.232	0.001	0.023	0.033	0.122
Cr	0.000	0.000	0.023	0.000	0.002	0.000	0.017	0.033	0.000
Ca	0.992	1.010	0.776	0.653	0.676	1.016	0.952	0.871	0.648
Mg	0.888	0.896	0.782	0.706	0.717	0.929	0.930	0.828	0.818
Mn	0.006	0.003	0.003	0.004	0.002	0.004	0.001	0.002	0.003
Ti	0.001	0.003	0.014	0.030	0.003	0.000	0.003	0.005	0.023
Al	0.011	0.088	0.301	0.469	0.185	0.009	0.009	0.298	0.389
Ni	0.001	0.001	0.002	0.001	0.002	0.001	0.001	0.000	0.000
Fe	0.076	0.043	0.089	0.300	0.195	0.072	0.043	0.085	0.223
Si	2.000	1.955	1.883	1.756	2.002	1.982	2.009	1.846	1.808
Total	3.978	4.000	4.008	4.038	4.016	4.014	3.988	4.001	4.034
^{IV}Al	0.000	0.045	0.117	0.244	0.000	0.018	0.000	0.154	0.192
^{VI}Al	0.011	0.043	0.184	0.225	0.185	-0.009	0.009	0.144	0.197
Vacancies	0.022	0.000	-0.008	-0.038	-0.016	-0.014	0.012	-0.001	-0.034

909 Note: The total Fe was calculated as FeO. The error of multi-point analysis is <1% for elements
910 with concentration >5% and <3% for elements with concentration >1%. The cations were
911 calculated based on 6 oxygen atoms except for the data for diopside (marble) which were from
912 Johnson et al. (2002). The vacancies were calculated as 4 minus total cations per 6 oxygen atoms.
913 The diopside-Aksu1 and diopside-Aksu2 have the same chemical composition, labeled as
914 diopside-Aksu in the table.

915

916

917

918

919

920

921

922

This is a preprint, the final version is subject to change, of the American Mineralogist (MSA)
Cite as Authors (Year) Title. American Mineralogist, in press.
DOI: https://doi.org/10.2138/am-2019-6661

923 **Table 2** Bulk and site-specific hydrogen diffusivities

Sample	Thickness (mm)	Temperature (°C)	Site-specific diffusivity ($log_{10}D$) Peak position (cm^{-1}) 3640	3620	3540	3520	3450	3360	Bulk diffusivity ($log_{10}D$)
Diopside-Russia	0.866	1000	-12.40 *±0.60*	-12.15 *±0.54*	/	-12.10 *±0.30*	-12.15 *±0.54*	/	-12.15 *±0.24*
Diopside-marble	0.212	1000	-12.30 *±0.30*	/	-12.00 *±0.22*	/	/	/	-12.22 *±0.18*
Diopside-JD	0.166	1000	-11.80 *±0.20*	/	-11.92 *±0.22*	/	-11.74 *±0.18*	/	-11.92 *±0.18*
Diopside-deep sea	0.146	1000	-11.70 *±0.30*	/	-12.00 *±0.22*	/	-11.74 *±0.18*	/	-12.00 *±0.26*
Augite-NS	0.980	1000	-11.30 *±0.30*	/	-11.10 *±0.20*	/	-11.52 *±0.48*	/	-11.22 *±0.18*
Diopside-Austria	0.759	1000	-10.60 *±0.22*	/	/	/	-10.70 *±0.30*	-10.55 *±0.19*	-10.80 *±0.20*

924

925

This is a preprint, the final version is subject to change, of the American Mineralogist (MSA)
Cite as Authors (Year) Title. American Mineralogist, in press.
DOI: https://doi.org/10.2138/am-2019-6661

Figure 1

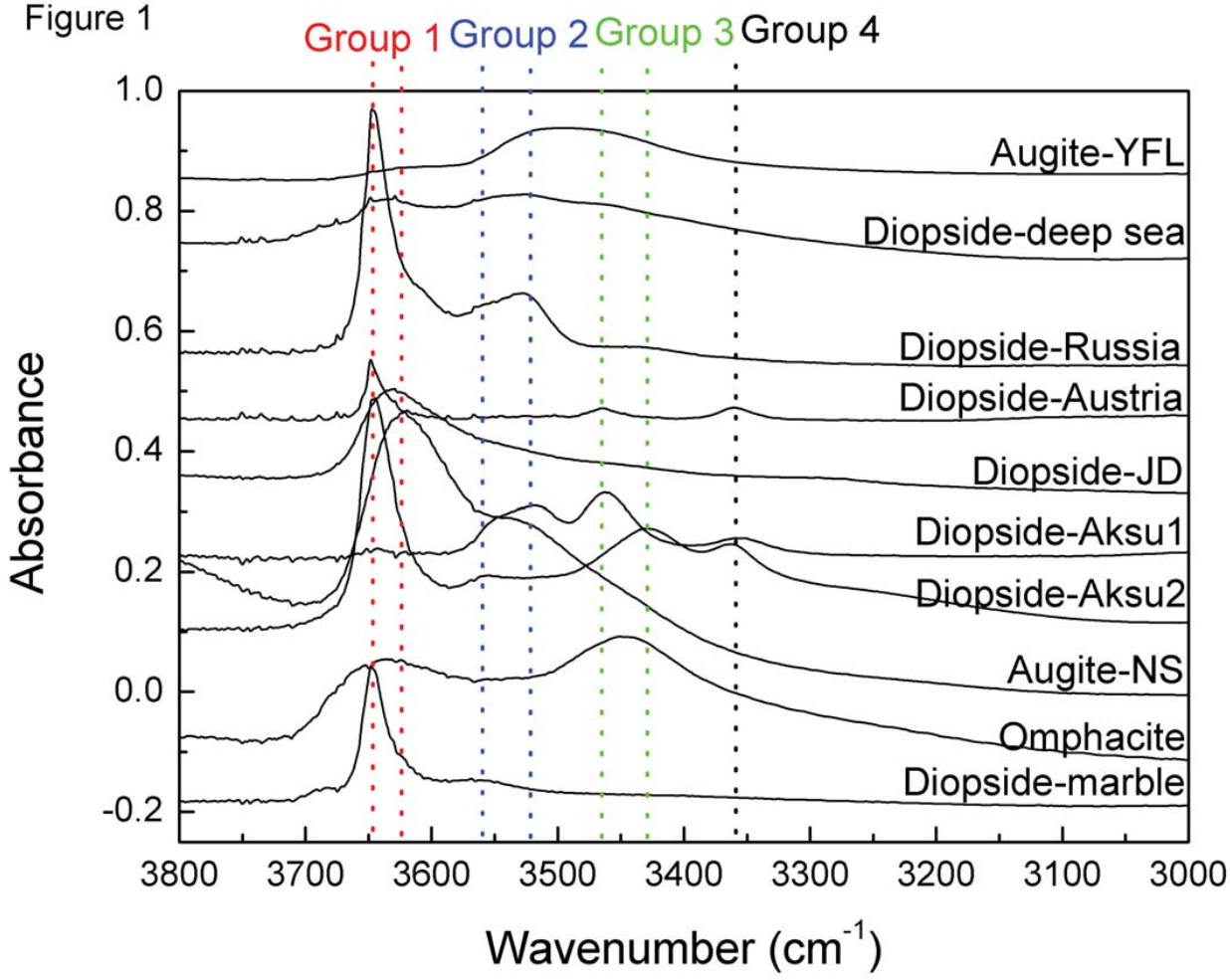

This is a preprint, the final version is subject to change, of the American Mineralogist (MSA)
Cite as Authors (Year) Title. American Mineralogist, in press.
DOI: https://doi.org/10.2138/am-2019-6661

Figure 2

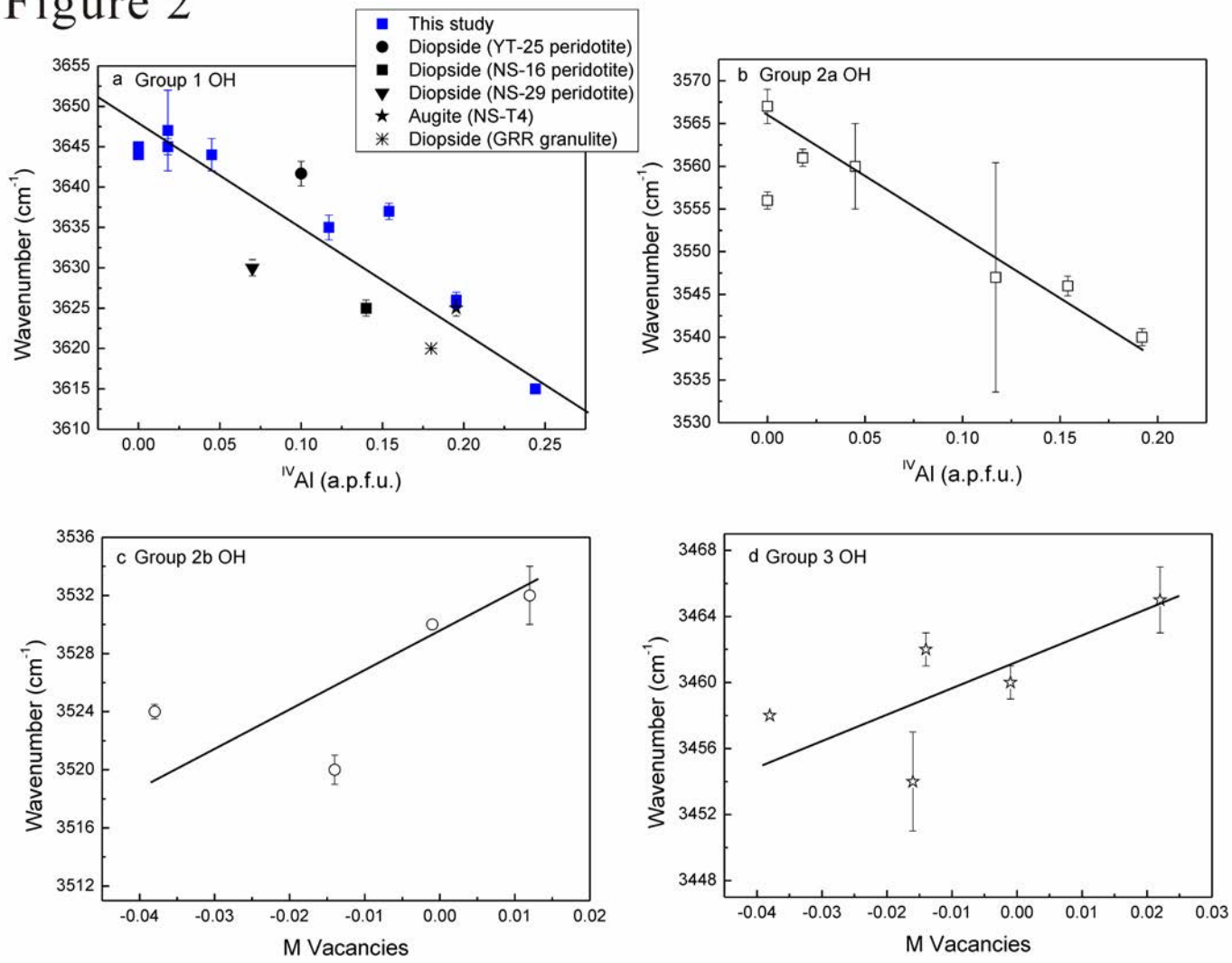

This is a preprint, the final version is subject to change, of the American Mineralogist (MSA)
Cite as Authors (Year) Title. American Mineralogist, in press.
DOI: https://doi.org/10.2138/am-2019-6661

Figure 3

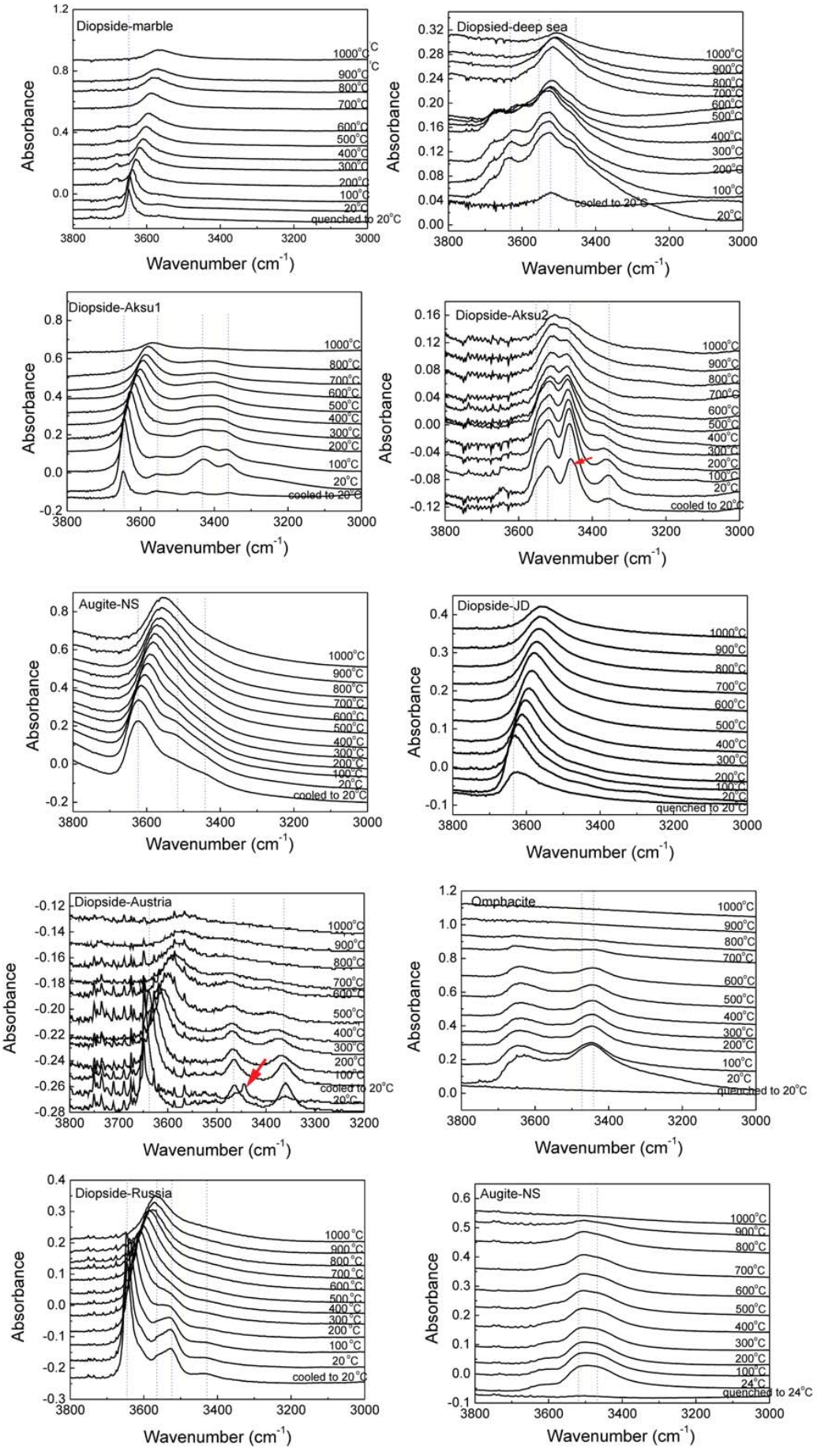

This is a preprint, the final version is subject to change, of the American Mineralogist (MSA)
Cite as Authors (Year) Title. American Mineralogist, in press.
DOI: https://doi.org/10.2138/am-2019-6661

Figure 4

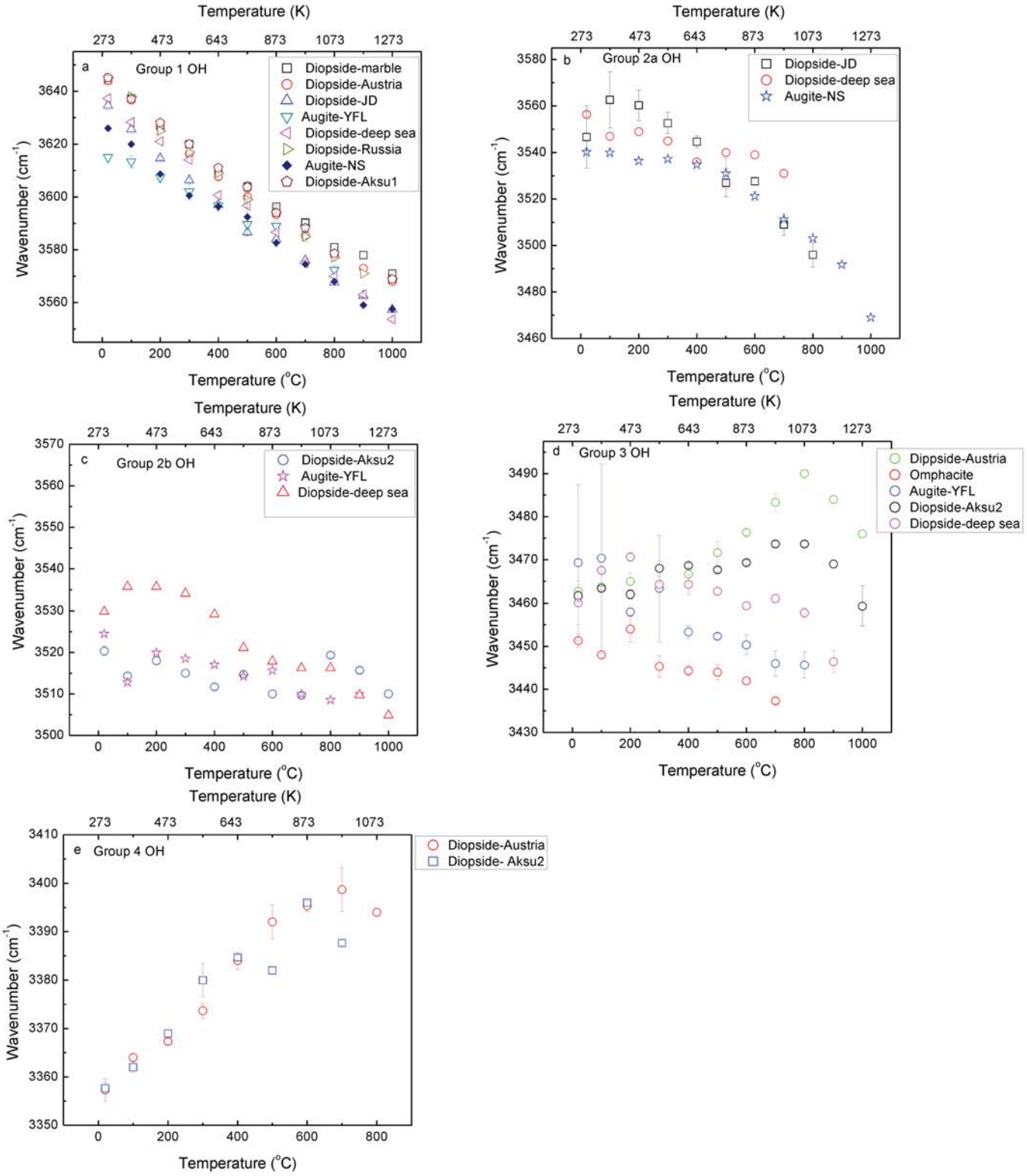

This is a preprint, the final version is subject to change, of the American Mineralogist (MSA)
Cite as Authors (Year) Title. American Mineralogist, in press.
DOI: https://doi.org/10.2138/am-2019-6661

Figure 5

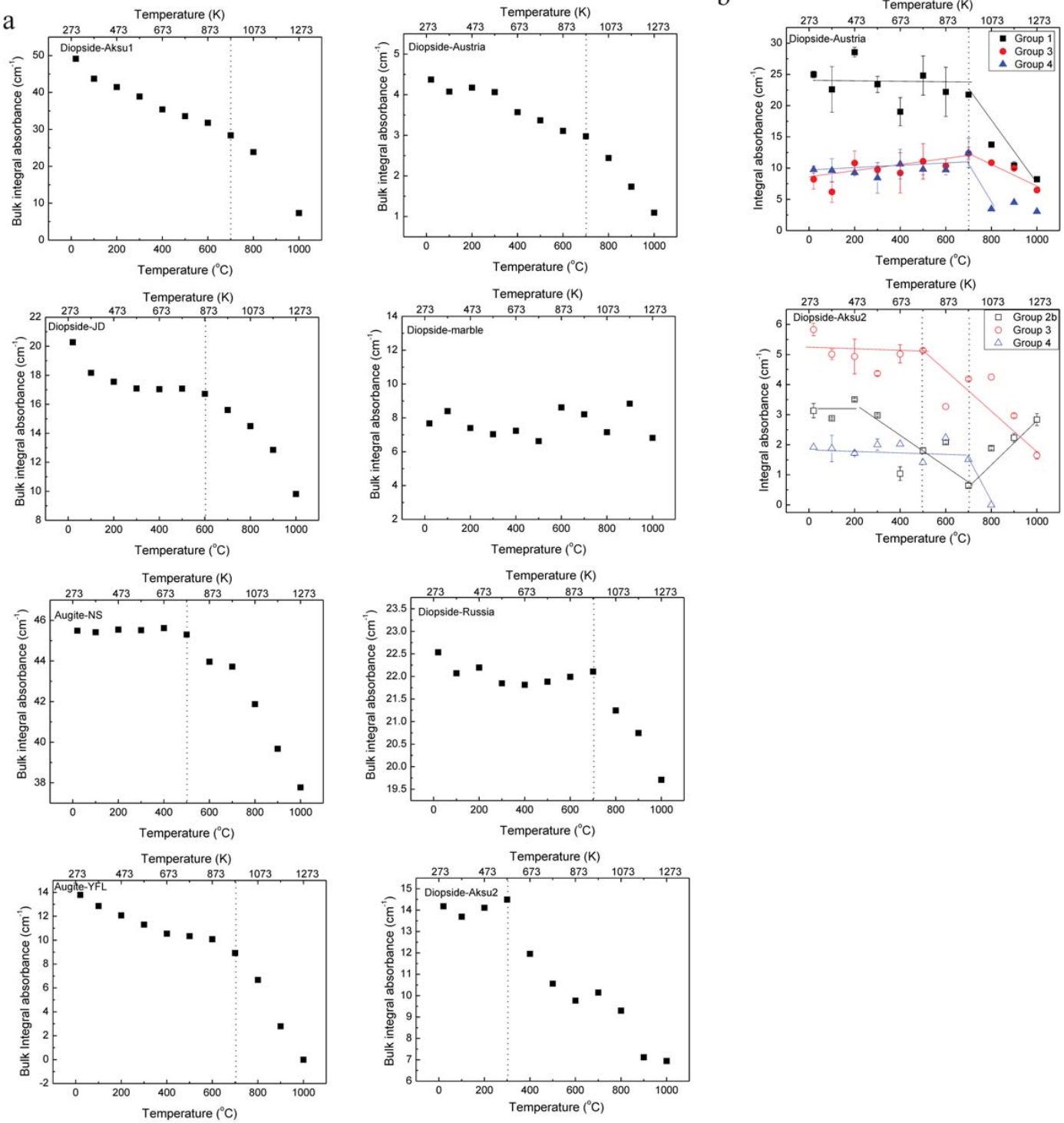

This is a preprint, the final version is subject to change, of the American Mineralogist (MSA)
Cite as Authors (Year) Title. American Mineralogist, in press.
DOI: https://doi.org/10.2138/am-2019-6661

Figure 6

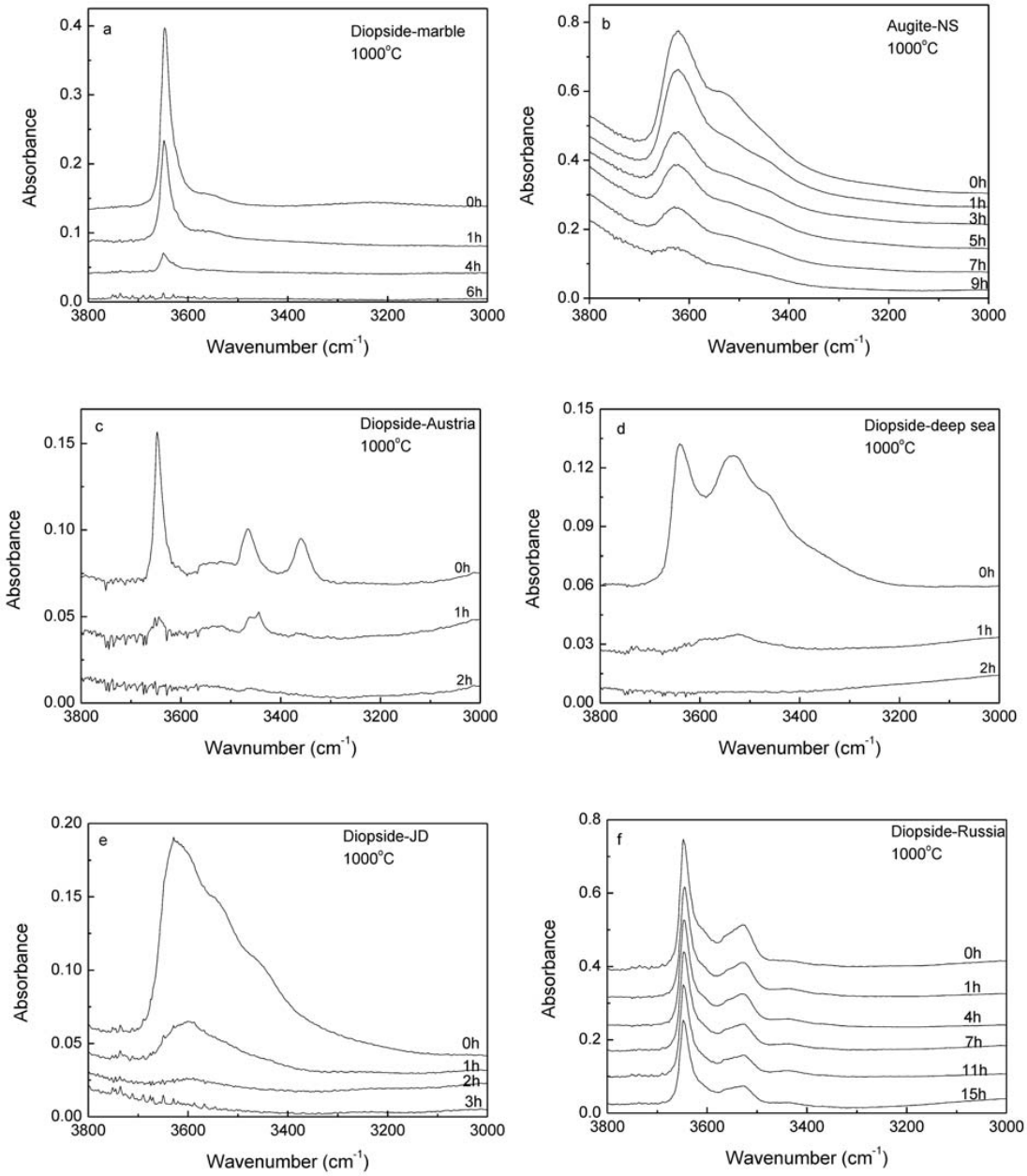

This is a preprint, the final version is subject to change, of the American Mineralogist (MSA)
Cite as Authors (Year) Title. American Mineralogist, in press.
DOI: https://doi.org/10.2138/am-2019-6661

Figure 7

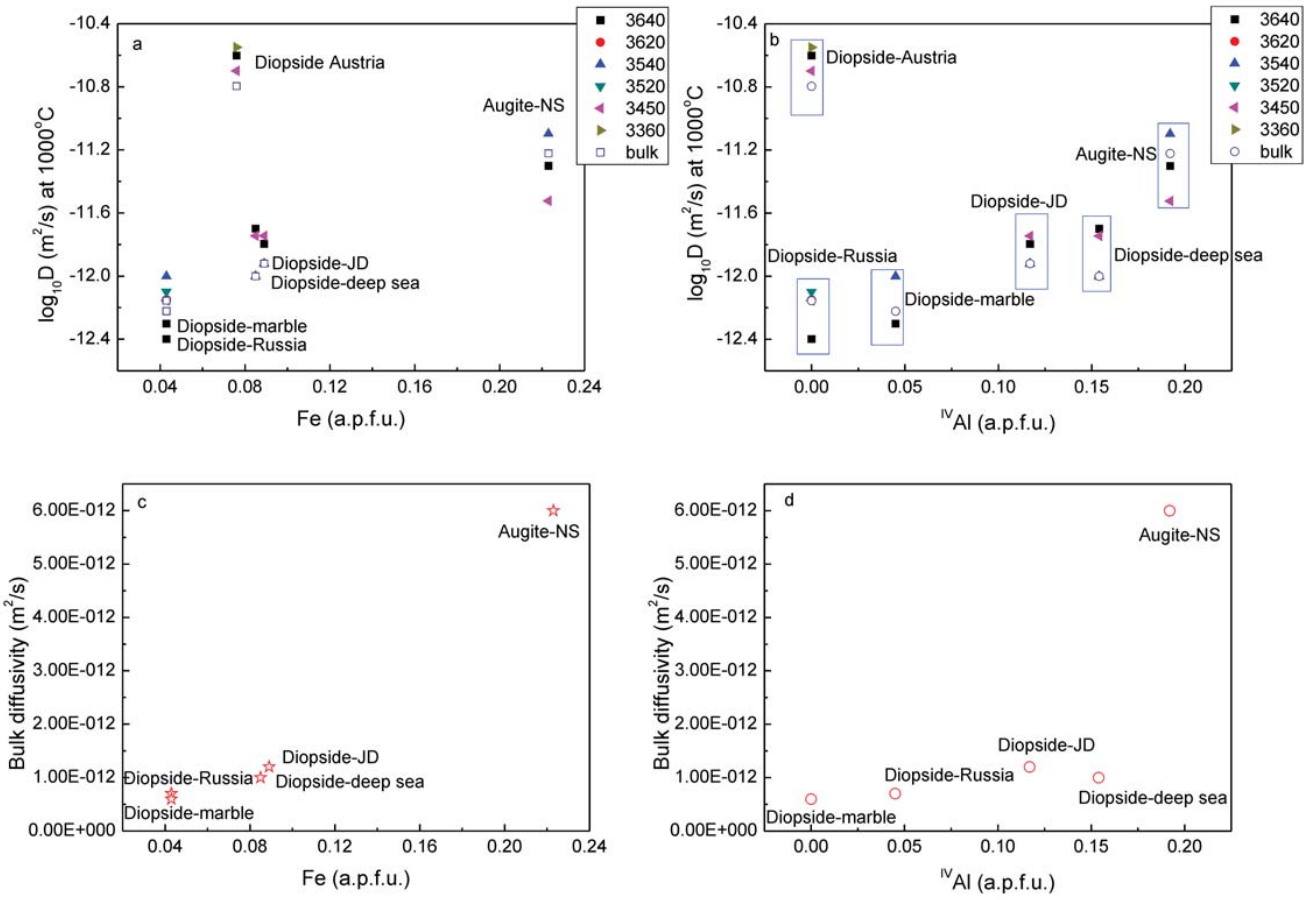

This is a preprint, the final version is subject to change, of the American Mineralogist (MSA)
Cite as Authors (Year) Title. American Mineralogist, in press.
DOI: https://doi.org/10.2138/am-2019-6661

Figure 8

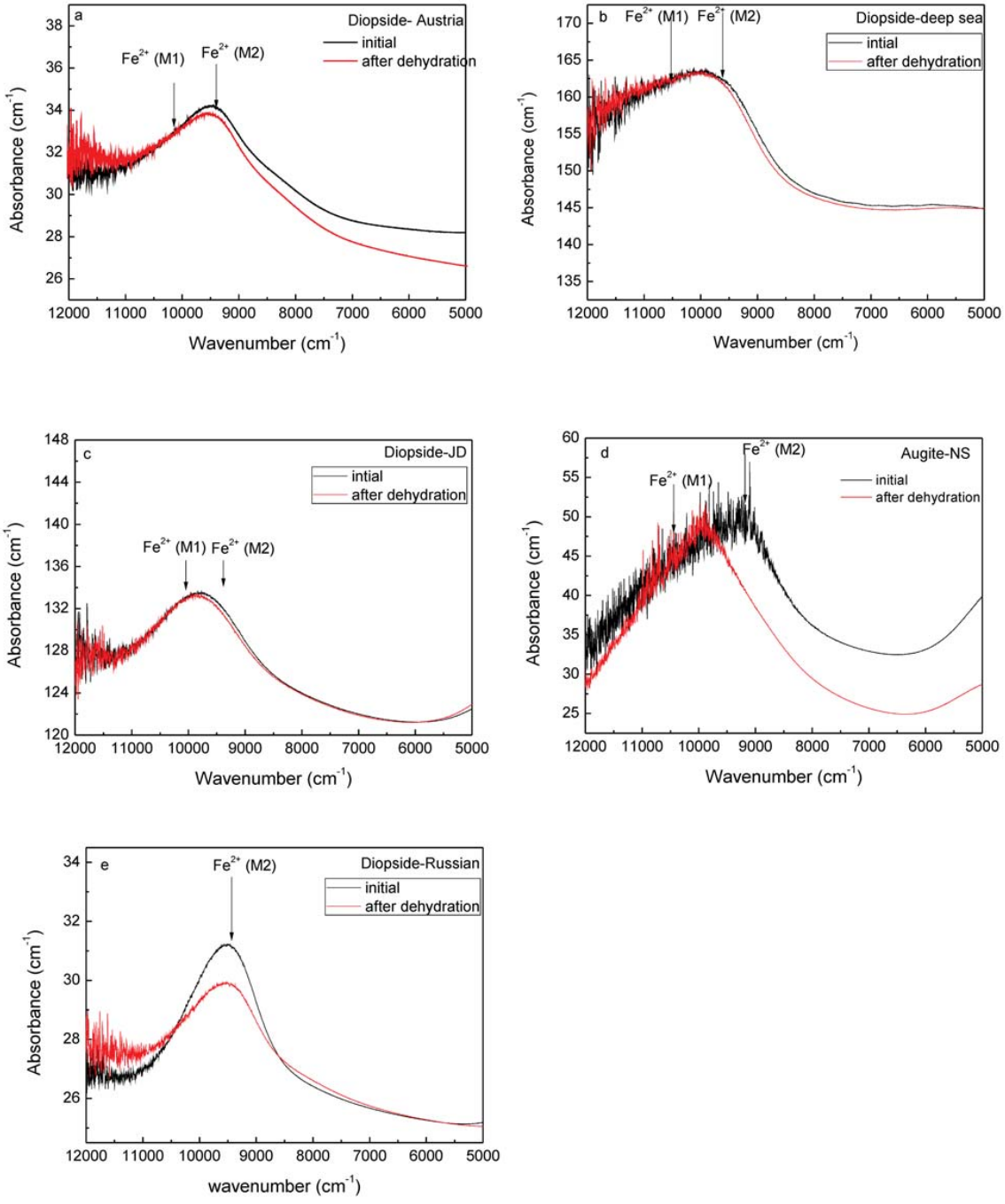

This is a preprint, the final version is subject to change, of the American Mineralogist (MSA)
Cite as Authors (Year) Title. American Mineralogist, in press.
DOI: https://doi.org/10.2138/am-2019-6661

Figure 9

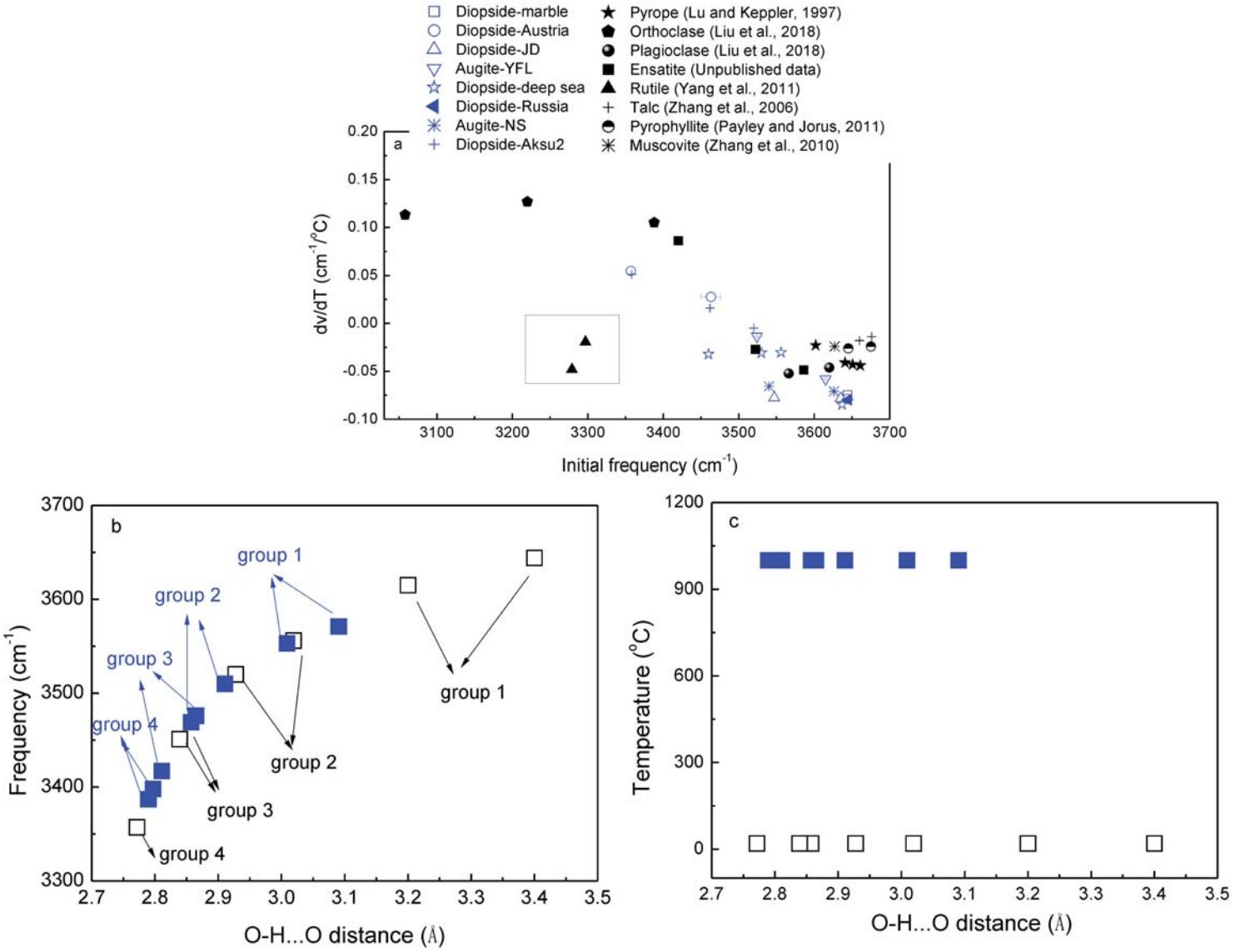

This is a preprint, the final version is subject to change, of the American Mineralogist (MSA)
Cite as Authors (Year) Title. American Mineralogist, in press.
DOI: https://doi.org/10.2138/am-2019-6661

Figure 10